metals

MDPI

Article

Effect of Sc, Hf, and Yb Additions on Superplasticity of a Fine-Grained Al-0.4%Zr Alloy

Aleksey V. Nokhrin *, Mikhail Yu. Gryaznov, Sergey V. Shotin, Galina S. Nagicheva, Mikhail K. Chegurov, Aleksandr A. Bobrov, Vladimir I. Kopylov and Vladimir N. Chuvil'deev

Materials Science Department, Lobachevsky State University of Nizhny Novgorod, Nizhny Novgorod 603022, Russia
* Correspondence: nokhrin@nifti.unn.ru

Abstract: This research was undertaken to study the way deformation behaves in ultrafine-grained (UFG)-conducting Al-Zr alloys doped with Sc, Hf, and Yb. All in all, eight alloys were studied with zirconium partially replaced by Sc, Hf, and/or Yb. Doping elements (X = Zr, Sc, Hf, Yb) in the alloys totaled 0.4 wt.%. The choice of doping elements was conditioned by the possible precipitation of Al_3X particles with $L1_2$ structure in the course of annealing these alloys. Such particles provide higher thermal stability of a nonequilibrium UFG microstructure. Initial coarse-grained samples were obtained by induction casting. A UFG microstructure in the alloys was formed by equal-channel angular pressing (ECAP) at 225 °C. Superplasticity tests were carried out at temperatures ranging from 300 to 500 °C and strain rates varying between 3.3×10^{-4} and 3.3×10^{-1} s^{-1}. The highest values of elongation to failure are observed in Sc-doped alloys. A UFG Al-0.2%Zr-0.1%Sc-0.1%Hf alloy has maximum ductility: at 450 °C and a strain rate of 3.3×10^{-3} s^{-1}, relative elongation to failure reaches 765%. At the onset of superplasticity, stress (σ)–strain (ε) curves are characterized by a stage of homogeneous (uniform) strain and a long stage of localized plastic flow. The dependence of homogeneous (uniform) strain (ε_{eq}) on test temperature in UFG Sc-doped alloys is increasing uniformly, which is not the case for other UFG alloys, with ε_{eq}(T) dependence peaking at 350–400 °C. The strain rate sensitivity coefficient of flow stress *m* is small and does not exceed 0.26–0.3 at 400–500 °C. In UFG alloys containing no Sc, the *m* coefficient is observed to go down to 0.12–0.18 at 500 °C. It has been suggested that lower *m* values are driven by intensive grain growth and pore formation in large Al_3X particles, which develop specifically at an ingot crystallization stage.

Keywords: aluminum; fine-gained alloys; doping; superplasticity; grain growth; diffusion

check for updates

Citation: Nokhrin, A.V.; Gryaznov, M.Y.; Shotin, S.V.; Nagicheva, G.S.; Chegurov, M.K.; Bobrov, A.A.; Kopylov, V.I.; Chuvil'deev, V.N. Effect of Sc, Hf, and Yb Additions on Superplasticity of a Fine-Grained Al-0.4%Zr Alloy. *Metals* **2023**, *13*, 133. https://doi.org/10.3390/met13010133

Academic Editors: Eric Hug and Andrey Belyakov

Received: 23 November 2022
Revised: 20 December 2022
Accepted: 29 December 2022
Published: 9 January 2023

Copyright: © 2023 by the authors. Licensee MDPI, Basel, Switzerland. This article is an open access article distributed under the terms and conditions of the Creative Commons Attribution (CC BY) license (https://creativecommons.org/licenses/by/4.0/).

1. Introduction

Avionic systems of modern aircraft are manufactured using thin composite wires made of low-doped aluminum alloys [1,2]. Such a modern aircraft onboard network is several kilometers long, which is why the replacement of copper wires with aluminum ones helps reduce the weight of an onboard network and improve the efficiency of aviation technology. Thin aluminum wires find applications in the automotive industry [3] and in the modern power industry [4]. Eutectic aluminum alloys with a high content of rare-earth elements (REEs) and commercial conductor Al-Mg-Si alloys are often used to produce wires [1,2,5,6]. The thermal stability of such commercial Al-REEs alloys and conventional Al-Mg-Si alloys is insufficient; therefore, many research teams are now actively engaged in designing novel heat-resistant, high-strength conductor aluminum Al-REEs alloys [6–14].

Specific requirements as to microstructure thermal stability and properties during long-term (several thousand hours) operation at 200–250 °C are imposed on thin aviation wires [1]. In this context, novel conductor dispersoid-hardened Al alloys are being actively developed. Scandium is one of the most effective doping elements for aluminum [15–23],

but high prices for Al-Sc master alloys hold back its extensive use. In this regard, researchers are developing multicomponent conductor aluminum alloys with improved strength, electrical conductivity, and thermal stability ensured by cheaper REEs and transition metals (TM) (see [15,17], etc.).

The Al-Zr system is one of the most popular for conductor aluminum alloys [24–31], but disadvantages of zirconium include low diffusibility of Zr atoms in aluminum [32–34] and discontinuous precipitation of a solid solution during annealing of Al-Zr alloys [35–39]. Therefore, Al-Zr alloys are often additionally doped with some other elements that accelerate the diffusibility of Zr atoms. Most often, Al-Zr alloys are doped with X = Er, Hf, Yb, Y, Si, Ti, W, etc. [40–66]. This allows for the precipitation of $Al_3(Zr,X)$ particles of variable composition at lower temperatures compared to precipitation temperatures of Al_3Zr particles. The wires are made by deformation (rolling, drawing, etc.), and precipitation of $Al_3(Zr,X)$ nanoparticles at low temperatures ensures better thermal stability of an ultrafine-grained (UFG) microstructure of a deformed aluminum alloy [67,68].

Currently, researchers are focused on studying the mechanical properties and electrical conductivity of conductor aluminum alloys at room temperature. The deformation behavior of conductor aluminum alloys at elevated temperatures remains under researched, although the deformation of an aluminum workpiece in most cases takes place at elevated temperatures. There are many scientific papers on the superplasticity of fine-grained conductor 6XXX Al alloys [69–78], but only few works on Mg-free UFG Al-1%Zr alloys [79] and Al-0.5%Mg-Sc alloys [80,81]. Optimal temperatures and strain rates will help to produce aluminum wires with a minimum number of breaks. An optimized composition of conducting aluminum alloys can bring down the number of breaks by reducing the number and size of primary Al_3Zr particles formed during the crystallization of Al-Zr-X alloys.

This study focuses on Al-Zr-Sc, Al-Zr-Hf, and Al-Zr-Yb alloys, as well as alloys simultaneously alloyed with several doping elements. Precipitation of $Al_3(Zr,Sc)$ and $Al_3(Zr,Hf)$ secondary particles in Al-Zr-(Sc,Hf) alloys is still more intensive at lower temperatures compared to Al_3Zr in Al-Zr alloys [15,40,43,45,68]. Therefore, during low-temperature heating, it is possible to ensure precipitation of a larger volume fraction of $Al_3(Zr,X)$ secondary particles compared to that of Al_3Zr particles. The low solubility of ytterbium (Yb) in molten aluminum at ordinary crystallization temperatures [82–85] and low solubility of Yb in Al at room and medium temperature [86,87] helps to obtain alloys with precipitated fine primary Al_3Yb particles [88]. Of note, secondary precipitation of $Al_3(Yb,Zr)$ and $Al_3(Yb,Sc)$ secondary particles is still more intensive at lower temperatures compared to Al_3Zr and Al_3Sc precipitates [41,56,89–93]. Thus, it is possible to make a fine-grained aluminum microstructure more stable at low annealing temperatures, as well as to further refine an ingot macrostructure. It should be noted that a large volume fraction of strong primary particles and their large size can lead to wire breaks during low-temperature rolling and drawing. Therefore, in this research, we limited the concentration of doping elements (no more than 0.4 wt.%), which was designed based on the results of previous studies.

The high stability of a UFG microstructure in aluminum alloys at lower heating temperatures allows for stable properties of thin wires operating at 200–250 °C [7,8,43,67,68]. Moreover, the stability of a nonequilibrium UFG microstructure at low temperatures will enable the low-temperature superplasticity effect in UFG aluminum alloys [69–76,80,81]. Raising the ductility of aluminum alloys while reducing their optimal deformation temperatures can help to increase the energy efficiency of production, in particular to reduce the number of breaks during the manufacturing of thin wires and to reduce the wear of equipment used in wire manufacturing. A drop in deformation temperatures and a rise in the rate of manufacture of thin bimetallic wires helps to further reduce the intensity of copper diffusion into the surface of an aluminum wire and, as a result, to reduce the intensity of brittle intermetallic compounds formation at the Al/Cu interface [68,94–96].

This study aims to research the deformation behavior of UFG conductor aluminum alloys at elevated temperatures.

2. Materials and Methods

Aluminum alloys with the content of doping elements totaling 0.4 wt.%, which corresponds to the solubility limit of zirconium in aluminum in selected induction casting modes, are investigated in this study. The chemical composition of the alloys under investigation is presented in Table 1.

Table 1. Aluminum alloys: chemical composition and casting modes.

Alloy No.	Doping Elements, wt.%/at.% [1]					Casting Modes
	Zr	Sc	Hf	Yb	∑	
1	0.4	-	-	-	0.4	Argon purging before melting: 3 cycles Argon purging during heating: 3 cycles Induction stirring Cooling: 50–250 s, under vibration Time to melt: 6–10 min Melt temperature: 800 °C Holding time before pouring: 60 min Pouring temperature: 760 °C
	0.118	-	-	-	0.118	
2	0.3	0.1	-	-	0.4	
	0.089	0.167	-	-	0.255	
3	0.3	-	0.1	-	0.4	
	0.089	-	0.015	-	0.104	
4	0.3	-	-	0.1	0.4	
	0.089	-	-	0.016	0.105	
5	0.2	0.1	0.1	-	0.4	
	0.059	0.167	0.015	-	0.241	
6	0.2	-	0.1	0.1	0.4	
	0.059	-	0.015	0.016	0.090	
7	0.2	0.1	-	0.1	0.4	
	0.059	0.167	-	0.016	0.242	
8	0.1	0.1	0.1	0.1	0.4	
	0.030	0.167	0.015	0.016	0.228	

[1]—numerator–concentration of doping elements (wt.%), denominator–calculated concentration of doping elements (at.%).

Aluminum alloy workpieces of 20 × 20 × 160 mm were obtained by vacuum induction casting in the modes indicated in Table 1. An Indutherm VTC 200 V vacuum casting machine (Indutherm GmbH, Walzbachtal, Germany) was used to produce ingots that were cast in a copper mold of 22 × 22 × 160 mm. A 150 cm^3 ceramic crucible was used. Alloys were made from aluminum A99, and master alloys such as Al-10%Zr, Al-2%Sc, Al-2.5%Yb, and Al-3%Hf were obtained by induction casting, followed by rolling into a foil 0.2 mm thick.

Equal-channel angular pressing (ECAP) was used to form a UFG microstructure in aluminum alloys. A detailed description of this technology can be found in [97,98]. ECAP helps to form a homogeneous UFG microstructure in aluminum alloy ingots, the parameters of which are close to those of a microstructure of a thin aluminum wire (see [67,68]). The above workpieces were subjected to 4 ECAP cycles to form a UFG microstructure. ECAP was performed at 250 °C using a Ficep HF400L hydraulic press (Ficep® S.P.A., Varese, Italy). Pressing was arranged using square-section tooling, with a channel intersection angle of 90°. ECAP was performed without billet rotations at a strain rate of 0.4 mm/s.

The resulting flat dogbone-shaped specimens with a working part of 2 × 2 × 3 mm were subjected to mechanical tests. Tensile tests were conducted using a Tinius Olsen H25K-S machine (Tinius Olsen Ltd., Surrey, UK) at a strain rate of 3.3 × 10^{-3} s^{-1} (tensile rate of 10^{-2} mm/s). Tests were run at temperatures ranging from 20 to 500 °C. During tests, a stress (σ)–strain (ε) curve was registered and used to determine ultimate tensile strength (σ_b) and elongation to failure (δ). Three specimens were tested at the above temperatures and strain rates.

An alloy microstructure was studied with a Leica DM IRM metallographic microscope (Leica Microsystems GmbH, Wetzlar, Germany), a Jeol JSM-6490 scanning electron microscope (SEM, Jeol Ltd., Tokyo, Japan), and a Jeol JEM-2100F transmission electron microscope (TEM, Jeol Ltd., Tokyo, Japan). Specimens were preliminarily subjected to mechanical grinding and polishing, as well as electropolishing (3 A, 30 V) for 1 min in CrO_3 + H_3PO_4 electrolyte. An alloy microstructure was exposed by etching in a solution of

HF (15 mL) + HNO_3 (10 mL) + glycerol (35 mL). The fractographic analysis that followed tensile tests was performed using a Jeol JSM-6490 SEM. The microstructure of specimens after tensile tests was studied using a Leica IM DRM metallographic microscope. Microhardness (HV) was measured using a Qness A60+ hardness tester (Qness GmbH, Golling, Austria) under a 50 g load. The average accuracy of HV measurement was ±15 MPa.

3. Results

3.1. Initial State Characterization

Cast alloys have a homogeneous macrostructure with large columnar crystals. The length of columnar crystals in the central part of thin sections may reach several millimeters. Along the edges of thin sections, there is an area of equiaxed grains, the average size of which is 10–50 μm, which leads to a fairly large spread of microhardness values registered in the center and along the edge of a thin section. No significant differences in macrostructures of alloy specimen Nos. 1–8 were observed.

The microstructure of cast and UFG alloys contains primary particles, the size and composition of which depend on the chemical composition of an alloy. Alloys doped with 0.3 and 0.4% Zr have single-micron Al_3Zr particles. UFG alloy Nos. 4, 6, 7, and 8 after ECAP have a large amount of light spherical and elongated flat Al_3Yb particles (Figure 1c–f). Single particles of a complex composition containing Fe, Si, and Ni can be observed in all the alloys; some particles have oxygen in their composition (Figure 1).

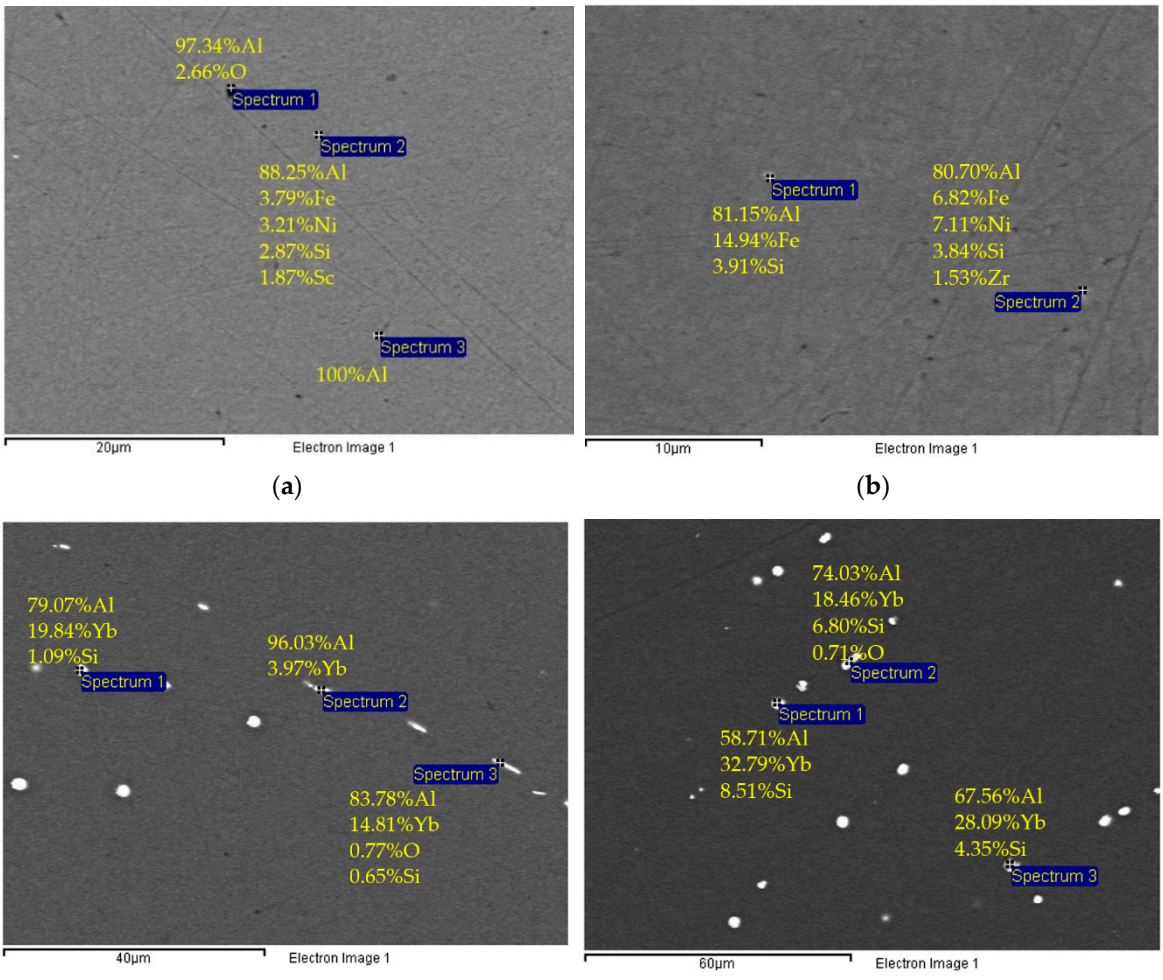
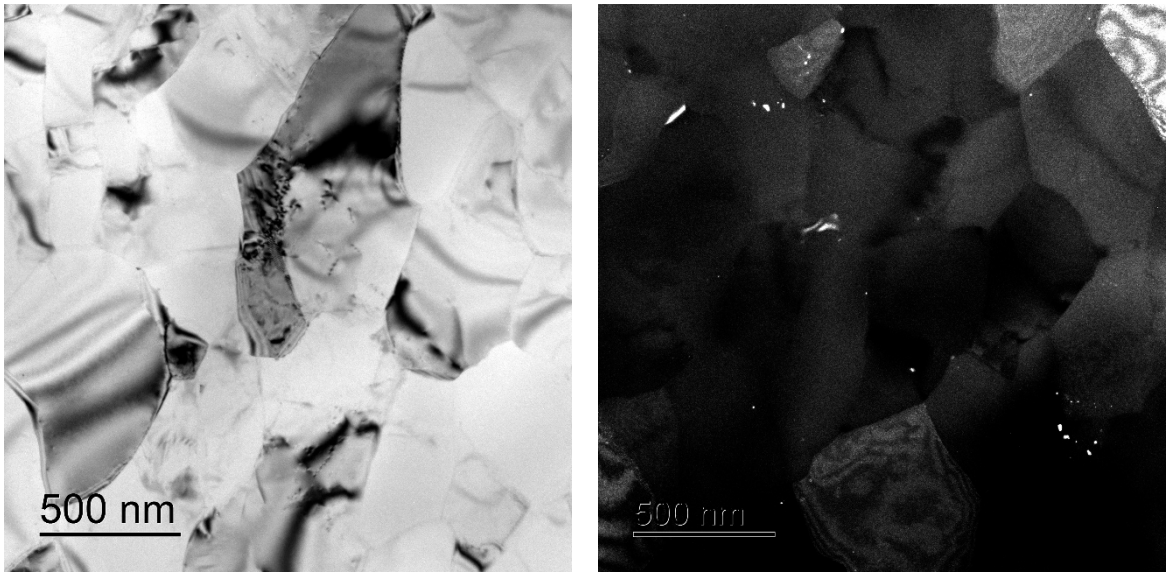


Figure 1. EDS analysis (wt.%) of particles in UFG alloy specimen Nos. 2 (**a**), 3 (**b**), 4 (**c**), and 6 (**d**). SEM.

The microstructure of UFG alloys is typical of severely deformed metals; the average fragment size is close to 0.5 μm (Figure 2a). No significant differences in the microstructure parameters of UFG alloy Nos. 1–8 were observed. No abnormally large grains were found in the microstructure of UFG alloys. A dark-field TEM image shows primary $Al_3(Zr,X)$ nanoparticles that were breaking down at an ingot crystallization stage (Figure 2b).



(**a**) (**b**)

Figure 2. Bright-field (**a**) and dark-field (**b**) images of UFG alloy No. 5 microstructure after ECAP. TEM.

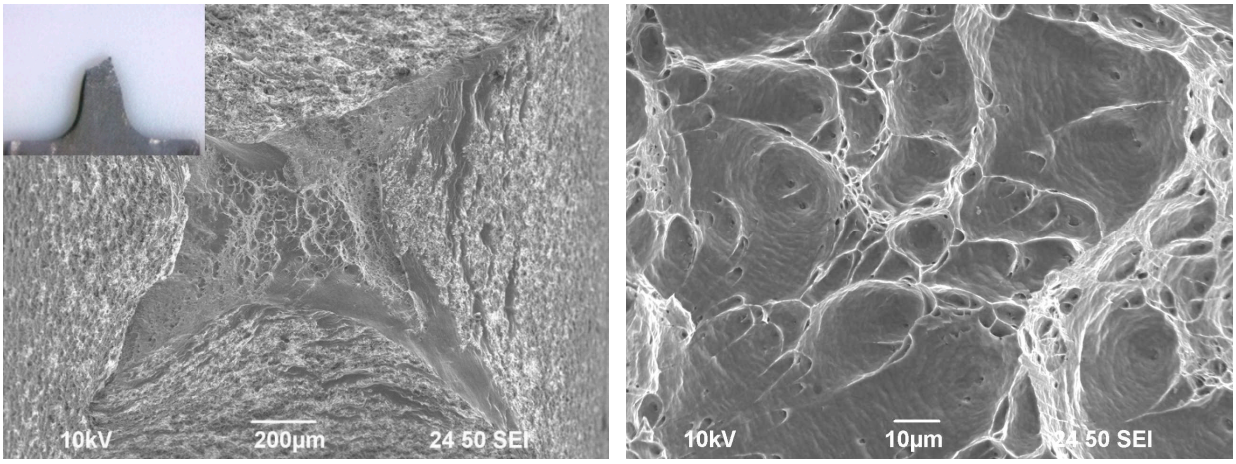
Table 2 presents the results of studying the mechanical properties of UFG alloy specimens. σ(ε) curves are typical of highly deformed materials; strain hardening is almost immediately followed by strain localization. Maximum ultimate tensile strength values (σ_b = 140–145 MPa) are observed in UFG alloy Nos. 2, 5, and 8. Relative elongation to failure in most UFG alloys is 15–20% (see Table 2).

Table 2. Mechanical properties of UFG alloys at room temperature.

Alloy No.	σ_b, MPa	δ, % [1]	HV, MPa
1	115	15–20	410 ± 10
2	140	20–25	455 ± 15
3	115	20–25	385 ± 15
4	125	15–20	410 ± 10
5	145	25–30	465 ± 10
6	125	20–25	415 ± 10
7	135	20–25	480 ± 20
8	140	20–25	455 ± 10

[1]—Relative elongation to failure was determined by changes in the length of a gage zone of a specimen after tensile tests.

Figure 3 shows the results of the fractographic analysis of UFG alloy No. 5 specimens. The results of the fractographic analysis of the remaining specimens are presented in Appendix A. According to the classification provided in [99], fractures that occur in specimens after tensile tests at room temperature are characterized by ductility (Figure 3a, see Appendix A). Specimens during tensile tests are destroyed to form a localization zone (see photographs of specimens in the upper left corner of Figure 3a). The central zone of fractures has dimples of various sizes (Figure 3b). UFG alloys characterized by increased strength and high elongation to failure have smaller dimples as compared to other UFG alloys (see Appendix A).

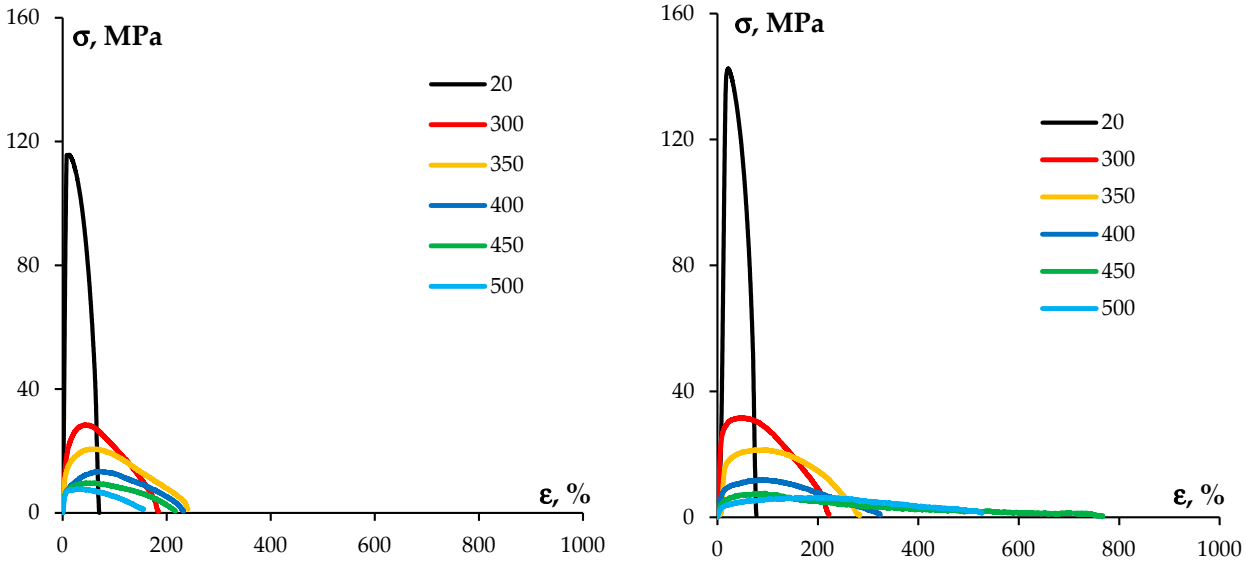


(**a**) (**b**)

Figure 3. SEM images of fracture surfaces in specimen No. 5 after tensile tests at room temperature. (**a**) offers a general view of the fracture, while (**b**) shows an enlarged image of the central part of the fracture.

3.2. Tests at Elevated Temperatures

Figure 4 and Appendix B show the stress (σ)–strain (ε) curves in UFG alloys at elevated tensile test temperatures. The σ(ε) tensile curves at low tensile temperatures (300–350 °C) are characterized by a pronounced stage of strain hardening, followed by a stage of localized plastic deformation. A uniform plastic flow stage is very short (Figure 4). With an increase in test temperatures, flow stress decreases, and elongation to failure in UFG alloys increases (Table 3). At test temperatures of 400–500 °C, the σ(ε) curves for UFG Sc-doped alloys have all the signs of superplastic flow: flow stress is very low, while elongation to failure exceeds several hundred percent (Table 3, Figure 4b). The σ(ε) curves for UFG Sc-doped alloy Nos. 2, 5, 7, and 8 show long stages of uniform plastic flow, followed by a long stage of localized plastic flow (Figure 4b, Appendix B).



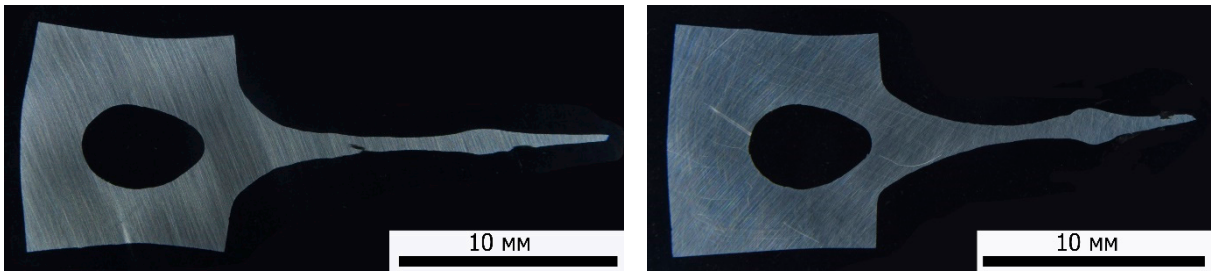
(**a**) (**b**)

Figure 4. σ(ε) curves in UFG alloys: series Nos. 1 (**a**) and 5 (**b**). Tests at elevated temperatures (°C) and a strain rate of 3.3×10^{-3} s^{-1}.

Table 3. Tensile tests of UFG alloys at elevated temperatures and a strain rate of 3.3×10^{-3} s^{-1}.

Alloy No.	300		350		400		450		500	
	σ_b, MPa	δ, %	σ_b, MPa	δ, %	σ_b, MPa	δ, %	σ_b, MPa	δ, %	σ_b, MPa	δ, %
1	47 ± 2	185 ± 10	20 ± 2	240 ± 20	14 ± 1	230 ± 20	10 ± 0.5	215 ± 20	8 ± 0.5	155 ± 15
2	53 ± 4	195 ± 10	20 ± 1	255 ± 20	11 ± 0.5	475 ± 25	7 ± 0.5	400 ± 30	5 ± 0.3	685 ± 40
3	28 ± 2	190 ± 10	23 ± 1	180 ± 15	15 ± 1	215 ± 15	9 ± 0.5	145 ± 15	7 ± 0.5	150 ± 15
4	31 ± 2	190 ± 10	27 ± 2	185 ± 15	17 ± 1	185 ± 15	9 ± 0.5	135 ± 10	9 ± 0.5	135 ± 10
5	31 ± 2	220 ± 15	21 ± 1	280 ± 25	12 ± 0.5	325 ± 25	8 ± 0.5	765 ± 40	6 ± 0.5	525 ± 40
6	38 ± 3	185 ± 10	26 ± 2	175 ± 15	16 ± 1	145 ± 10	13 ± 1	155 ± 15	7 ± 0.5	155 ± 15
7	30 ± 1	210 ± 20	20 ± 1	295 ± 25	11 ± 1	455 ± 30	8 ± 0.5	360 ± 35	9 ± 0.5	250 ± 20
8	31 ± 2	260 ± 20	21 ± 2	265 ± 15	12 ± 1	325 ± 25	8 ± 0.5	385 ± 30	7 ± 0.5	320 ± 30

At a localized plastic deformation stage, necking is observed in the gage zone of a specimen. Several localized deformation zones occur in Sc-doped alloys at 500 °C (Figure 5). Intense formation of localized deformation zones is generally observed at elevated temperatures and low strain rates.



(**a**) (**b**)

Figure 5. Specimens after superplasticity tests: (**a**) alloy No. 2 (500 °C, 1×10^{-3} s^{-1}); (**b**) alloy No. 5 (500 °C, 3.3×10^{-4} s^{-1}).

The results of tensile tests of UFG alloys at elevated temperatures are presented in Table 3.

Data in Table 3 show that elongation to failure nonmonotonically (with a peak) depends on test temperatures; flow stress decreases monotonically along with an increase in test temperatures. The highest superplasticity is registered in Sc-doped alloy Nos. 2, 5, 7, and 8 (Table 3). At 400 °C and a strain rate of 3.3×10^{-3} s^{-1}, maximum elongation to failure (δ = 455–475%) is observed in UFG alloy Nos. 2 and 7 (Table 3). UFG alloy No. 5 has maximum ductility at elevated temperatures: at 450 °C and a strain rate of 3.3×10^{-3} s^{-1}, elongation to failure reaches 765% (Table 3). UFG alloy No. 2 also has high superplastic characteristics: at 500 °C and a strain rate of 3.3×10^{-3} s^{-1}, elongation to failure reaches 685%.

Figure 6 shows the dependence of uniform strain (ε_{eq}) on test temperature in UFG alloys. When a long stage of uniform plastic flow appeared on the σ(ε) curve, ε_{eq} was taken as deformation corresponding to an early stage of strain localization (onset of stress reduction).

It is noteworthy that based on the nature of ε_{eq}(T) dependence, all UFG alloys can be divided into two large groups. Alloy No. 1, 3, 4, and 6 with low ductility at elevated temperatures (400–500 °C) (Table 3) display a nonmonotonic ε_{eq}(T) dependence. Figure 6 shows that ε_{eq}(T) dependence in UFG alloy Nos. 1, 3, 4, and 6 reaches its maximum at 350–400 °C. With a further increase in test temperatures, ε_{eq} decreases. It stands to mention that maximum uniform strain values for UFG alloy Nos. 1, 3, 4, and 6 are small and do not exceed 70–90% (Figure 6). ε_{eq}(T) dependence in UFG alloy Nos. 2, 5, 7, and 8 is different: with an increase in test temperatures, there is a monotonic increase in ε_{eq}. UFG alloy No. 2 is an exception since it demonstrates a slight decrease in ε_{eq} at 500 °C (Figure 6), but the scale of this decrease only slightly exceeds ε_{eq} error.

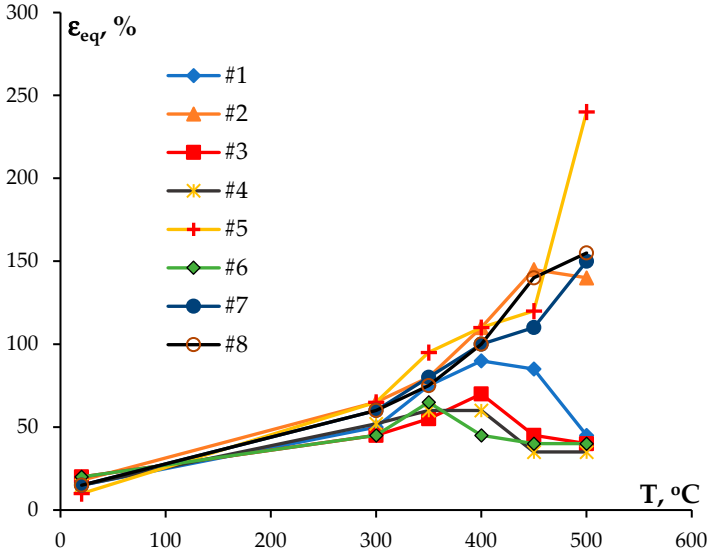


Figure 6. Dependence of homogeneous (uniform) strain on test temperatures in UFG alloys.

The effect of strain rate on the results of superplasticity tests was studied at 400 and 500 °C. The test results are presented in Table 4. The analysis of data in Table 4 shows that an increase in strain rates triggers an increase in flow stress, which is a common effect in the superplasticity tests of fine-grained materials [100]. Elongation to failure nonmonotonically (with a peak) depends on the test temperatures of UFG aluminum alloys (Table 4). In the region of high-strain-rate superplasticity at a strain rate of 3.3×10^{-1} s^{-1}, elongation to failure in UFG aluminum alloys reaches 105–160% at 400 °C, while at 500 °C for some UFG alloys, δ is close to 200% (Table 4). At higher strain rates, uniform deformation (ε_{eq}) is small, and a localized deformation stage is mostly observed on σ(ε) curves (Figure 7). Figure 8 shows that the higher the strain rate, the shorter the stage of localized deformation and the higher the flow stress.

Table 4. Results of tensile tests of UFG alloy specimens at elevated temperatures and strain rates. Numerator–flow stress (MPa), denominator–elongation to failure (%).

Alloy No.	T = 400 °C				T = 500 °C			
	3.3×10^{-4}	3.3×10^{-3}	3.3×10^{-2}	3.3×10^{-1}	3.3×10^{-4}	3.3×10^{-3}	3.3×10^{-2}	3.3×10^{-1}
1	-	14 ± 0.5	25 ± 1	-	-	8 ± 0.5	11 ± 0.5	14 ± 1
	-	230 ± 20	130 ± 10	-	-	155 ± 10	160 ± 15	180 ± 15
2	7 ± 0.5	11 ± 0.5	26 ± 1	-	3 ± 0.2	5 ± 0.3	13 ± 1	-
	335 ± 30	475 ± 35	280 ± 20	-	435 ± 35	685 ± 35	385 ± 25	-
3	-	15 ± 1	34 ± 2	45 ± 2	-	7 ± 0.4	9 ± 0.5	13 ± 1
	-	215 ± 20	155 ± 15	105 ± 10	-	150 ± 10	200 ± 15	195 ± 15
4	-	17 ± 1	34 ± 2	47 ± 3	-	9 ± 0.5	11 ± 0.5	14 ± 1
	-	185 ± 15	150 ± 15	105 ± 10	-	135 ± 10	110 ± 10	150 ± 15
5	7 ± 0.5	12 ± 0.5	27 ± 2	-	5 ± 0.3	6 ± 0.3	11 ± 1	-
	340 ± 30	325 ± 25	235 ± 20	-	500 ± 30	525 ± 35	515 ± 35	-
6	-	16 ± 1	29 ± 2	35 ± 2	-	7 ± 0.4	10 ± 0.5	14 ± 1
	-	145 ± 15	130 ± 10	115 ± 10	-	155 ± 15	110 ± 10	150 ± 10
7	-	11 ± 0.5	24 ± 1	44 ± 3	-	9 ± 0.5	12 ± 1	29 ± 2
	-	455 ± 40	275 ± 30	160 ± 15	-	250 ± 25	440 ± 35	215 ± 15
8	-	12 ± 1	21 ± 1	45 ± 3	-	7 ± 0.4	14 ± 1	30 ± 2
	-	325 ± 35	280 ± 25	135 ± 10	-	320 ± 30	300 ± 25	145 ± 10

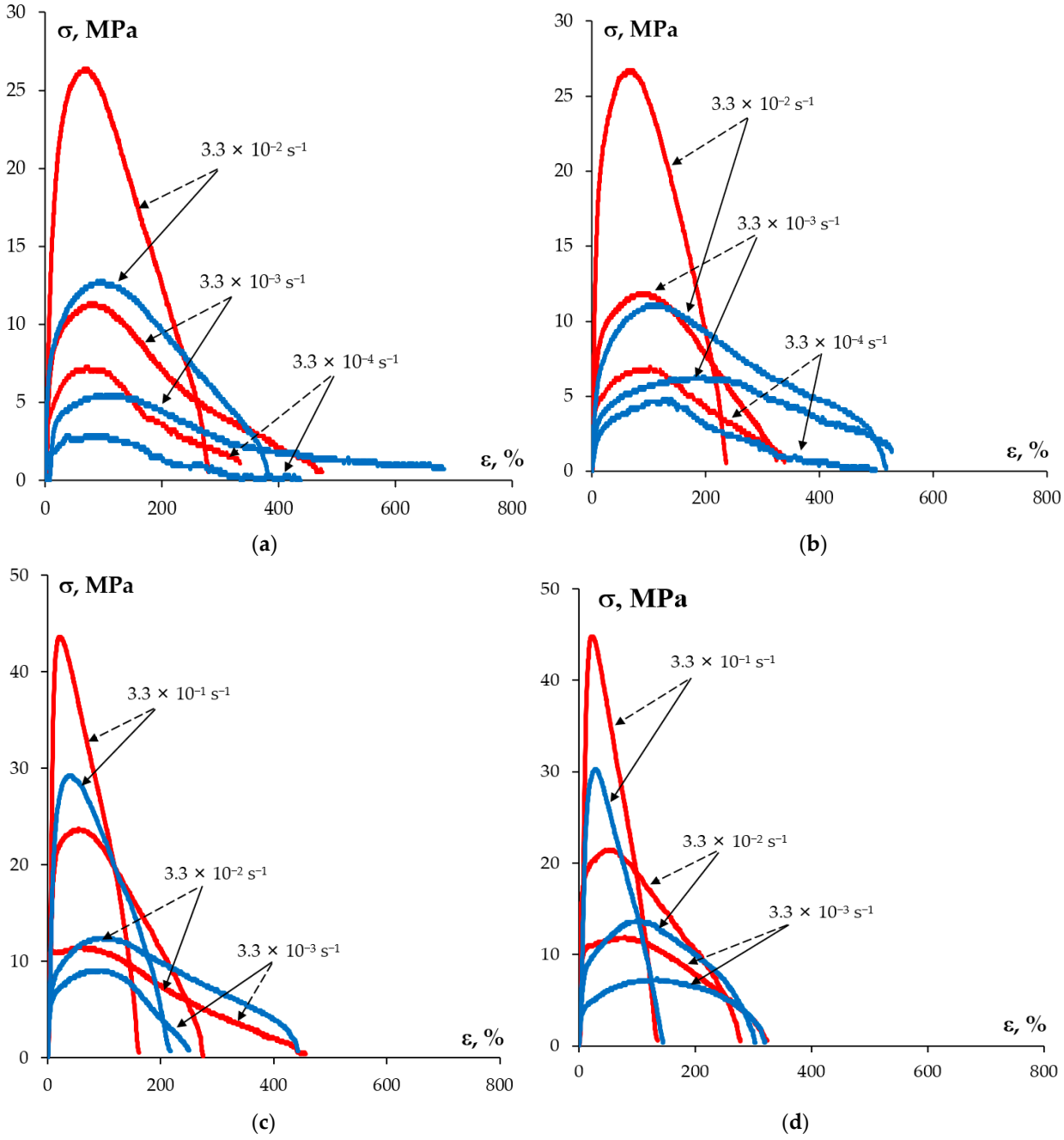


Figure 7. The effect of strain rate on σ(ε) curves in UFG alloy Nos. 2 (**a**), 5 (**b**), 7 (**c**), and 8 (**d**). Numbers near σ(ε) curves indicate strain rates at 500 °C.

Figure 8 and Appendix B show the results of the fractographic analysis of UFG alloy specimens after superplasticity tests at 400 and 500 °C. Fractures in all specimens are ductile in nature and represent a set of dimples of various sizes. With an increase in deformation temperatures, dimples diminish in size along with a cross-sectional area of fractures (Figure 8). UFG alloy specimens with increased ductility have an extremely small cross-sectional area of fractures; fractures show single dimples of 10–20 μm. A small cross-sectional area of fractures indirectly indicates a high strain localization, which corresponds to data concerning little uniform strain (ε_{eq}) in these alloys (Figure 8). Such a conclusion is underpinned by shape analysis of specimens after tensile tests, the photos of which are shown in the upper right corner of Figure 8 and in Appendix B. It should be noted that single dimples are visible in fractures of some specimens tested at 400 °C, with the size of

dimples reaching 50–100 μm (Appendix B). In our opinion, cavitation fracture is the reason for such defects.

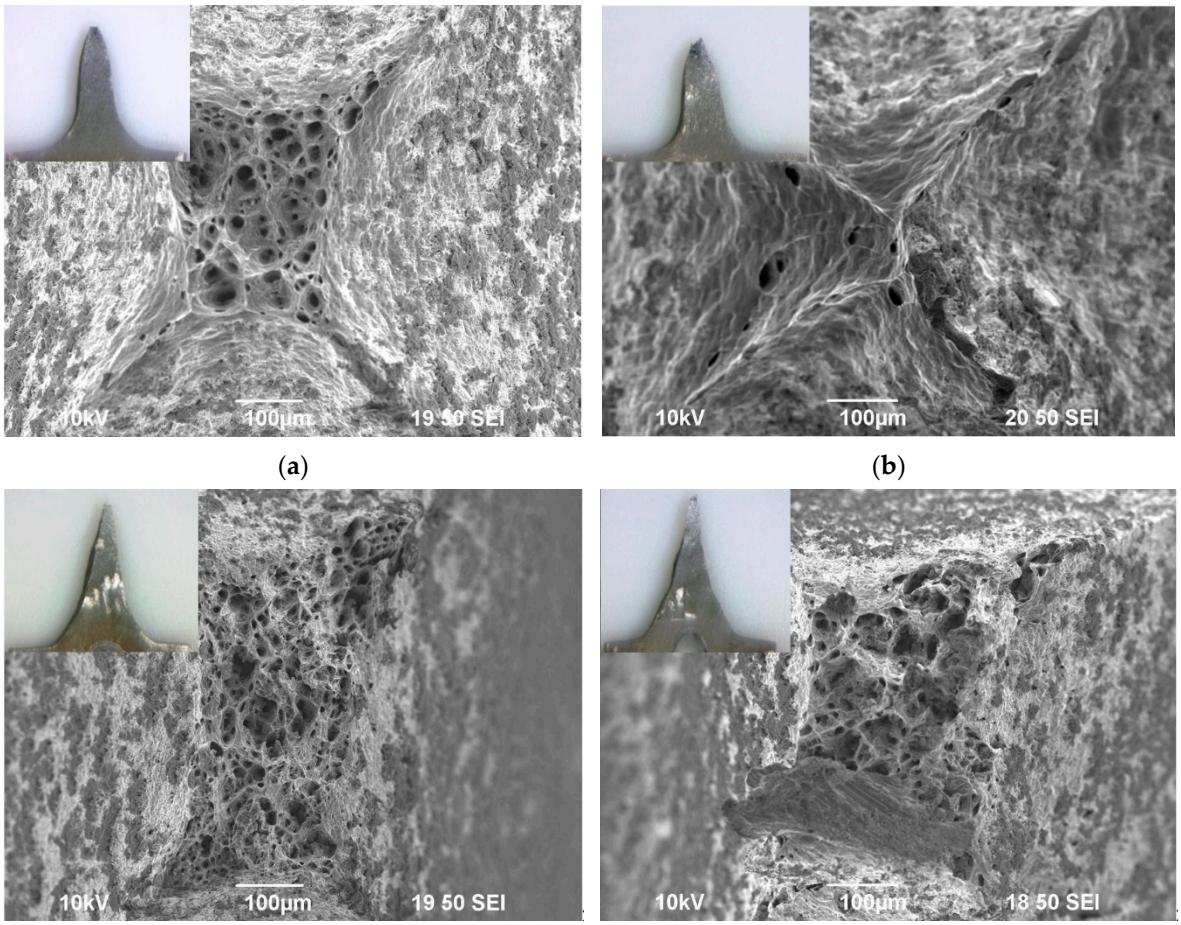


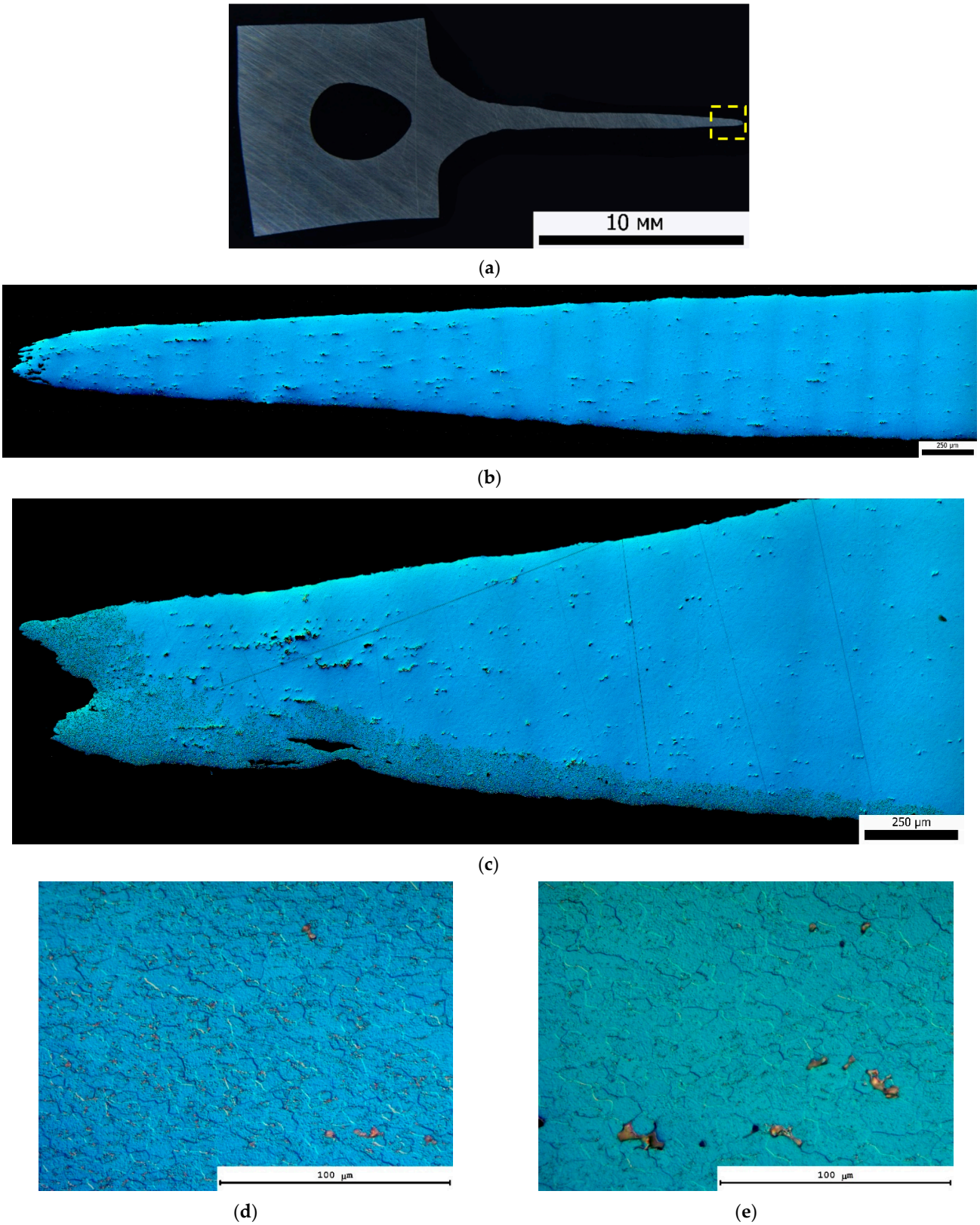
Figure 8. Fractographic analysis of UFG alloy specimens No. 1 (**a**,**b**) and No. 5 (**c**,**d**) after tensile tests at 400 °C (**a**,**c**) and 500 °C (**b**,**d**). Strain rate of 3.3×10^{-3} s^{-1}.

Figure 9 presents the results of the microstructure investigations of the UFG aluminum alloy samples from series #5 after the superplasticity tests with the strain rate of 3.3×10^{-3} s^{-1} at 450 °C and 500 °C. The samples of this series had the highest value of the elongation to failure (Table 2). The area of investigation is outlined by a yellow dashed line in Figure 9a.

The pores are seen on the sample surfaces after the tension tests, and the sizes and quantity of the pores increase near the destruction zone (Figure 9b,c). Note that according to the model [101], the presence of the secondary particles nucleating when heating the UFG aluminum alloy is the origin of the pore formation in the superplasticity conditions. The dislocation-disclination type defects forming around large secondary particles in the superplasticity conditions can lead to the acceleration of the cavitation destruction of the UFG alloys [102–105]. A similar effect was described earlier for the case of superplasticity of UFG conductor aluminum alloys Al-0.5%Mg-Sc [80,81].

Figure 9d,e presents the microstructure images of the UFG alloy samples near the destruction areas. This area is outlined by the yellow dashed line in Figure 9a. One can see in Figure 9d that the mean grain sizes in the destruction area in the samples after the superplasticity tests at 450–500 °C were ~10–15 μm. The mean grain sizes (d ~ 10–15 μm) exceeded the initial grain size in the UFG alloys (~0.5 μm) essentially. The result obtained evidences an intensive grain growth in the superplasticity conditions. Note that the grains

had the shapes close to the equiaxial ones while the pores were located preferentially at the grain boundaries (Figure 9d,e).



(**a**)

(**b**)

(**c**)

(**d**)

(**e**)

Figure 9. Macrostructure (**a**,**b**,**c**) and microstructure (**d**,**e**) of the samples from series No. 5 after the superplasticity tests at 450 °C (**a**,**b**,**d**) and 500 °C (**c**,**e**). The strain rate 3.3 × 10^{-3} s^{-1}.

4. Discussion

ECAP is an effective technology to form a UFG microstructure in aluminum alloys [97,98,106,107]. A distinct ECAP advantage is the opportunity to form a large fraction of high-angle grain boundaries (HAGBs) in a fine-grained material [98,106,107]. HAGBs in the microstructure of a fine-grained material help to launch the grain boundary sliding (GBS) effect, which, under optimal temperature–rate deformation conditions, is the main mechanism of the low-temperature superplastic deformation of fine-grained materials [100,108]. The third factor contributing to the higher superplastic characteristics of UFG alloys is the nonequilibrium state of their high-angle grain boundaries. As shown in [98,109–112], during ECAP, HAGBs accumulate dislocation defects, leading to an increase in the free volume of grain boundaries and a decrease in the activation energy of superplastic deformation. During the superplastic deformation of UFG alloys, their grain boundaries actively interact with lattice dislocations, thus triggering an increase in the free (excess) volume of high-angle grain boundaries [98,110–112]. Thus, ECAP provides all the necessary conditions conducive to the superplasticity effect in aluminum alloys. The superplasticity of UFG aluminum alloys produced by ECAP has been studied thoroughly in many works (see, for example, [80,81,106,113–117]); therefore, we will not dwell on their analysis. For the purposes of analyzing the results that we obtained, we should only emphasize that UFG-conducting aluminum alloys exhibit very good superplastic characteristics (Tables 3 and 4).

Let us analyze superplastic deformation in UFG-conducting aluminum alloys. The main rheological superplastic flow equation usually runs as follows [100,108]:

$$\dot{\varepsilon} = A(\sigma^*/G)^{1/m}(b/d)^p(D_{eff}/b^2)(G\Omega/kT) \quad (1)$$

where m is the strain rate sensitivity coefficient of flow stress, the value of which depends on strain rate $\dot{\varepsilon}$ (m is usually 0.5 under optimal superplasticity conditions); p is a numerical parameter equal to 2 or 3 [109]; b is the Burgers vector; G is the shear modulus; k is the Boltzmann constant; σ^* is flow stress; and D_{eff} is the effective diffusion coefficient under superplasticity conditions. It is usually assumed that $\sigma^* = \sigma_b$, $D_{eff} = D_0\exp(Q_{eff}/kT)$, where Q_{eff} is the effective activation energy of superplastic flow. Q_{eff} is usually close to grain boundary diffusion activation energy Q_b [108], but in the case of UFG metals, it often turns out to be less than Q_b [98,110,111], and in the case of multiphase materials or in the case of diffusion creep, it can be greater than Q_b [100].

The rheological superplasticity equation can also be presented in such a way that contributions of intergranular ($\dot{\varepsilon}_b$) and intragranular deformation ($\dot{\varepsilon}_v$) are separated:

$$\dot{\varepsilon} = \dot{\varepsilon}_b + \dot{\varepsilon}_v \quad (2)$$

To describe the grain boundary sliding (GBS) rate $\dot{\varepsilon}_b$, the following equation is usually used:

$$\dot{\varepsilon}_b = A_b(\sigma/G)^2(b/d)^2(G\Omega/kT)\left(\delta D_b/b^3\right) \quad (3)$$

where A_b is a numerical coefficient equal to ~100 [98,108]. To calculate intragranular strain rate $\dot{\varepsilon}_v$, the usual equation for strain rate under power-law creep [100,108] is used.

The strain rate sensitivity coefficient of flow stress $m = \ln(\sigma_b)/\ln(\dot{\varepsilon})$ can be determined by the slope of flow stress–strain rate dependence in logarithmic coordinates. These dependencies in the UFG aluminum alloys under study are shown in Figure 10. The charts provided herein show that rather low m values that do not exceed 0.26–0.30 are observed in all alloys at 400 and 500 °C (Figure 10). Such results prove that the selected temperature–rate modes of UFG alloy deformation are not optimal.

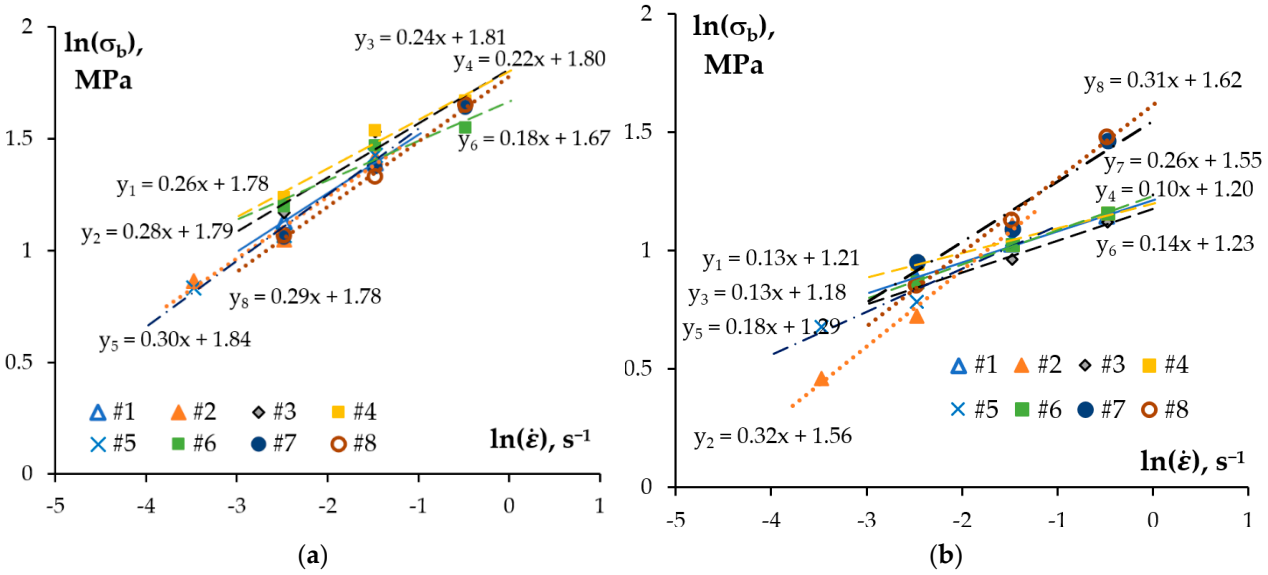


Figure 10. Dependencies of flow stress on strain rate in UFG alloys at 400 °C (**a**) and 500 °C (**b**).

It is worth noting that the values of the *m* coefficient in most UFG alloys at 500 °C are somewhat lower than at 400 °C. The *m* values for Sc-doped alloys turn out to be close to each other at 400 and 500 °C. This is rather unexpected, since higher elongations to failure are observed at elevated temperatures (Tables 3 and 4). We reckon that there are two main reasons why the superplastic deformation modes of UFG-conducting aluminum alloys are suboptimal at elevated temperatures.

First, it should be pointed out that dynamic grain growth is observed in UFG aluminum alloys at elevated temperatures and strain rates (see Figure 9). According to Equations (1) and (3), this leads to a decrease in optimal superplastic strain rates, as well as to changes in strain hardening and an increase in flow stress [112–120]. Moreover, it must be mentioned that intensive dynamic grain growth leading to the formation of a coarse-grained microstructure is one of the main reasons for the higher strain hardening and lower elongation to failure of UFG materials under deformation at elevated temperatures.

It should be emphasized that UFG Sc-doped alloys exhibit the highest superplastic characteristics [80,81,114–118]. Al_3Sc particles and Sc-containing intermetallic compounds of variable composition with $L1_2$ structure are among the most effective stabilizers for a nonequilibrium UFG microstructure of aluminum alloys [18–21,121–124]. This suggests that UFG Sc-doped alloys have the lowest rate of dynamic grain growth and, as a consequence, the smallest grain size under superplasticity conditions. In accordance with (1), this allows for higher optimal strain rates and maximum superplastic characteristics of UFG alloys.

The second factor is secondary particles present in a UFG alloy microstructure, including relatively large primary particles formed at an ingot crystallization stage. Large strong particles trigger the acceleration of pore nucleation under superplastic deformation conditions [101] and consequently premature cavitation fracture in UFG alloys. According to a model provided in [101], pore nucleation occurs because dislocation glide is hugely impeded, and dislocations and disclinations emerge around particles. Cavitation fractures in UFG-conducting alloys under superplasticity conditions tally with the results of fractographic analysis (Figure 8, Appendix C). As noted above, one of the reasons for large pores on the fracture surfaces in UFG alloy specimens can be large particles in the failure zone. This conclusion indirectly agrees with the results of superplasticity tests. As can be seen from Tables 3 and 4, maximum elongation to failure is observed in UFG alloys with reduced Zr content. Large fan-shaped particles of Al_3Zr and Al_3Sc, which are often formed by discontinuous precipitation [33–39,80,81,124–127], can be one of the main factors for accelerated cavitation fracture in UFG alloys under superplasticity conditions. Cavitation

fracture accompanying superplasticity in UFG-conducting alloys with elevated Sc content was described in [80,81].

In conclusion, let us analyze the way the type and composition of secondary particles affect the superplasticity characteristics of UFG aluminum alloys. As shown above, the highest superplasticity characteristics are achieved in UFG Sc-doped alloys (Figure 11).

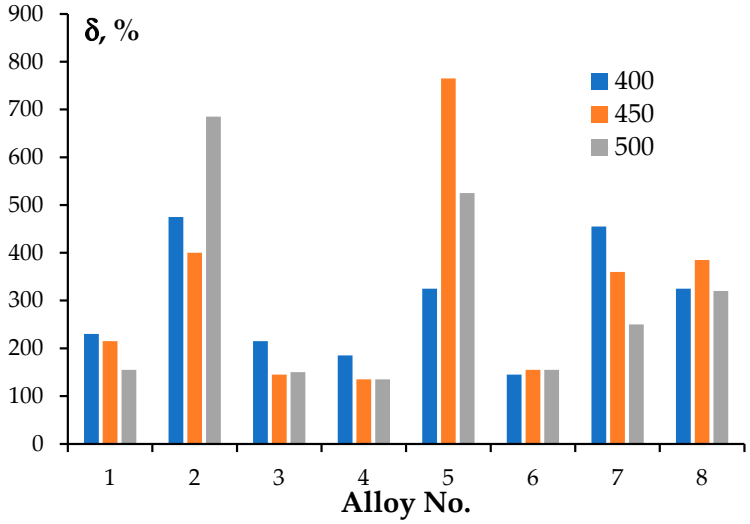


Figure 11. Elongation to failure in various alloys tested at 400, 450 and 500 °C. Strain rate of 3.3×10^{-3} s^{-1}.

When analyzing the results obtained, it should be borne in mind that Zr, Sc, Hf, and Yb have significantly different distribution coefficients in aluminum. The way doping elements are distributed in the alloy during crystallization can be described using distribution coefficient $K = C_S/C_L$, where C_S and C_L stand for concentrations of doping elements in the liquid and solid phases, respectively [128]. At $K < 1$, doping elements concentrate in the liquid phase during crystallization and form grain boundary segregations after crystallization. At $K > 1$, doping elements tend to concentrate in the grain volume during crystallization. At $K = 1$, doping elements are distributed evenly between grain boundaries (dendritic boundaries) and the volume of grains (dendritic volume). In aluminum, zirconium (K_{Zr} = 2.5–2.54 [128]) and hafnium (K_{Hf} = 4.0–6.01 [128]) are horophobic elements and, after crystallization, are predominantly found in the aluminum crystal lattice. Ytterbium in aluminum (K_{Yb} = 0.08 [128]) is a horophilic element and forms segregations along grain boundaries or dendritic boundaries. Scandium is uniformly distributed in aluminum (K_{Sc} = 0.9–1.0 [128]). Differences in the way doping elements are distributed can lead to differences in the way particles precipitate during the heating of UFG aluminum alloys.

The second factor that must be taken into account when analyzing the results is that due to differences in the atomic masses of Al (26.98 a.m.u.), Zr (91.224 a.m.u.), Sc (44.956 a.m.u.), Hf (178.49 a.m.u.), and Yb (173.044 a.m.u.), the concentration of Sc in at.% in the alloys under study significantly exceeds that of all other doping elements (Zr, Hf, and Yb) (Table 1). Therefore, in Sc-doped alloy Nos. 2, 5, 7, and 8, the volume fraction of precipitating (f_v) Al_3X particles will be noticeably higher than in other alloys (No. 1, 3, 4, and 6). Table 1 shows that alloy Nos. 2, 5, and 7 are expected to have the largest volume fraction of precipitated particles. A nonequilibrium UFG microstructure in Sc-doped alloys will stabilize better due to the Zener relation: $d_Z = \alpha_1 f_v/R$, where d_Z is the stable grain size, R is the particle size, and α_1 is a numerical coefficient depending on the particle shape [129]. The reduced ductility of Sc-doped alloy No. 7 compared with alloy Nos. 2 and 5 (Tables 3 and 4) stems from the fact that a big part of the total concentration of doping elements is made up of ytterbium atoms located along grain boundaries in the form of large primary Al_3Yb particles (Figure 2) and have little effect on stabilization of a UFG microstructure in the aluminum alloy. Alloys 3, 4, and 6 (Figure 11) with the

lowest total concentration of doping elements display the lowest superplasticity (minimum elongation to failure) (Table 1), and therefore, we can expect the smallest volume fraction of secondary particles.

It should be noted that in accordance with the data presented in Table 1, one would expect increased superplastic characteristics in UFG alloy No. 2, which has the highest total concentration of doping elements ($C_{\sum}$ = 0.241%). Figure 11 shows that at a deformation temperature of 450 °C, the highest values of elongation to failure are observed in UFG alloy No. 5 ($C_{\sum}$ = 0.255%). Elongation to failure in UFG alloy No. 2 at 450 °C is lower than in UFG alloy No. 5. We reckon that the reason for this effect lies in the difference in the chemical composition and structure of precipitated particles in alloy Nos. 2 and 5.

As shown in [130–132], precipitating secondary Al_3(Zr,Sc) particles in Al-Zr-Sc alloys have the following structure: Al_3Sc core–Al_3Zr shell. The diffusion coefficient of scandium in aluminum [133–136] is noticeably higher than the diffusion coefficient of zirconium in aluminum [32]. As a result, Al_3Sc particles precipitate at lower temperatures or shorter heating times compared to Al_3Zr particles. At higher temperatures or longer heating times, a stable Al_3Zr shell is formed on the surface of precipitated Al_3Sc nanoparticles. An elevated Sc concentration in alloy No. 2 will trigger the formation of Al_3Sc particles in the crystal lattice and along the grain boundaries of the aluminum alloy.

Doping Al-Zr alloys with hafnium is also known to accelerate the formation of secondary Al_3Zr particles, but higher temperatures are required [40,43,68]. In our opinion, doping Al-Zr-Sc alloy with Hf during heating leads to secondary Al_3(Hf,Zr) particles that are formed at higher temperatures compared to Al_3(Sc,Zr) and Al_3Sc particles. Thus, it becomes possible to ensure the thermal stability of a fine-grained microstructure of Al-0.2%Zr-0.1%Sc-0.1%Hf alloy in a wide range of temperatures and strain rates. Small grain size in the alloys under study, in accordance with (1), leads to an increase in optimal rates of superplastic deformation and to an increase in the ductility of alloy No. 5.

5. Conclusions

1. This research focused on the superplastic characteristics of ultrafine-grained (UFG) conducting Al-Zr alloys doped with Sc, Hf, and Yb with a total content of doping elements not more than 0.4 wt.%. It was shown that the partial replacement of zirconium with rare-earth elements and other transition metals allows for higher ductility of UFG alloys at elevated temperatures. UFG alloys containing 0.1% Sc exhibit the highest superplasticity. A UFG Al-0.2%Zr-0.1%Sc-0.1%Hf alloy has maximum ductility: at 450 °C and a strain rate of 3.3×10^{-3} s^{-1}, its relative elongation to failure reaches 765%. A UFG Al-0.3%Zr-0.1%Sc alloy also has high superplastic characteristics: at 500 °C and a strain rate of 3.3×10^{-3} s^{-1}, its relative elongation to failure reaches 685%.

2. It was shown that at a deformation temperature of 400 °C, the strain rate sensitivity coefficient of flow stress (m) values are 0.26–0.28. An increase in deformation temperatures to 500 °C leads to a decrease in m values. The reason for low m values is dynamic grain growth and pore nucleation in large Al_3(Zr,X) particles.

Author Contributions: Conceptualization, A.V.N.; methodology, A.V.N.; validation, A.V.N. and V.N.C.; formal analysis, A.V.N. and V.N.C.; investigation, M.Y.G., S.V.S., G.S.N., M.K.C., A.A.B., V.I.K.; resources, A.V.N. and V.N.C.; data curation, A.V.N.; writing—original draft preparation, A.V.N.; writing—review and editing, A.V.N. and V.N.C.; visualization, A.V.N.; supervision, A.V.N.; project administration, A.V.N.; funding acquisition, A.V.N. All authors have read and agreed to the published version of the manuscript.

Funding: This research was supported by the Russian Science Foundation (Gant No. 20-19-00672). The investigations of the microstructure of the alloys by TEM were carried out using the instrumentation of the Center Collective Use "Materials Science and Metallurgy" (National University of Science and Technology "MISIS") supported by the Ministry of Science and Higher Education of the Russian Federation (Grant No. 075-15-2021-696).

Data Availability Statement: Not applicable.

Acknowledgments: The authors thank V. V. Zakharov (Russian Institute of Light Alloys, Moscow) for his recommendations on adjusting the composition of new conducting alloys and their casting modes. The authors thank N. Yu. Tabachkova (National University of Science and Technology "MISIS", Moscow) for TEM results.

Conflicts of Interest: The authors declare no conflict of interest.

Appendix A

Appendix A presents the results of fractographic analysis of UFG alloy specimens after testing at room temperature. A general view of the fracture (on the left) and an enlarged image of the central part of the fracture (on the right) are presented for each specimen.

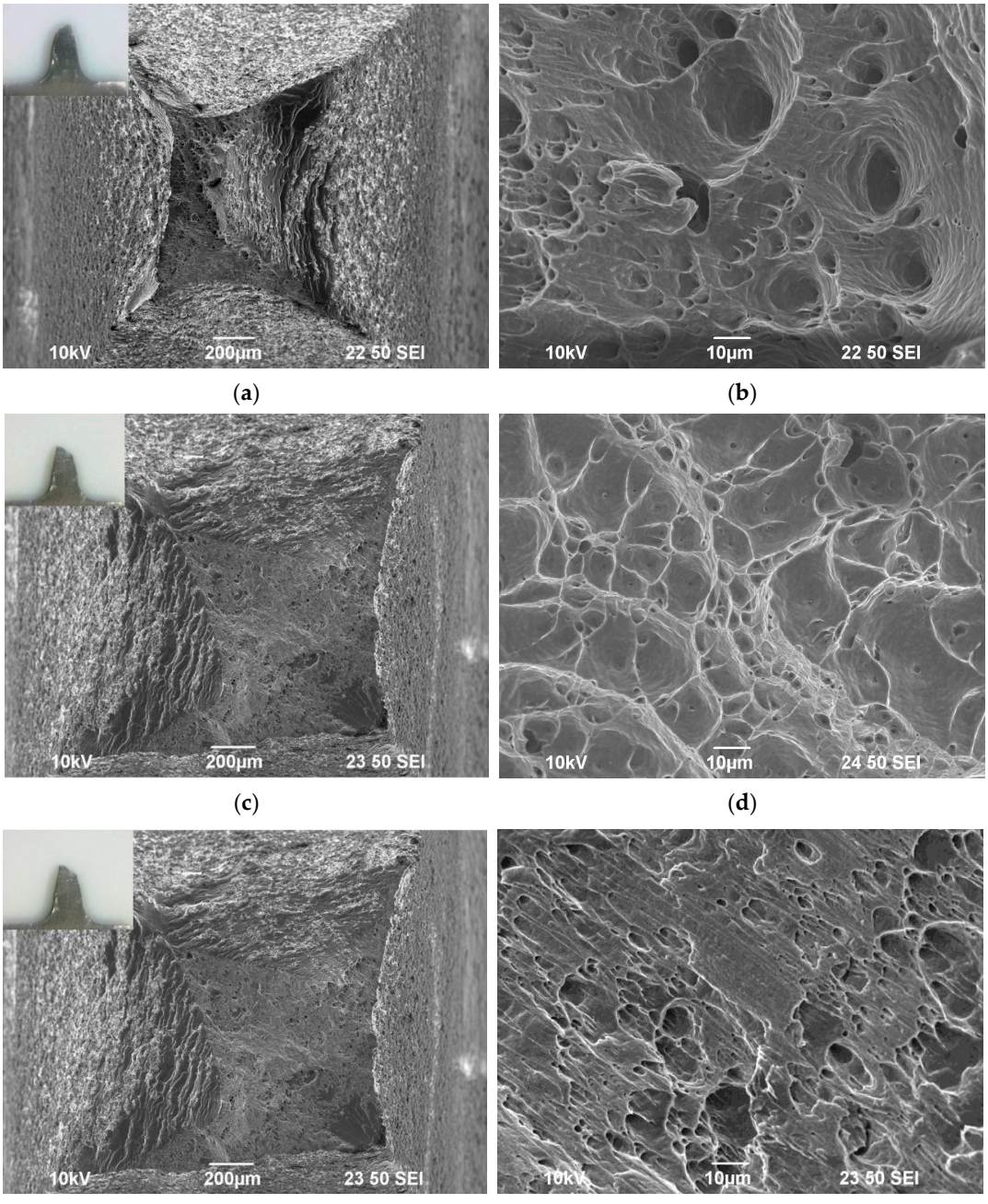


Figure A1. *Cont.*

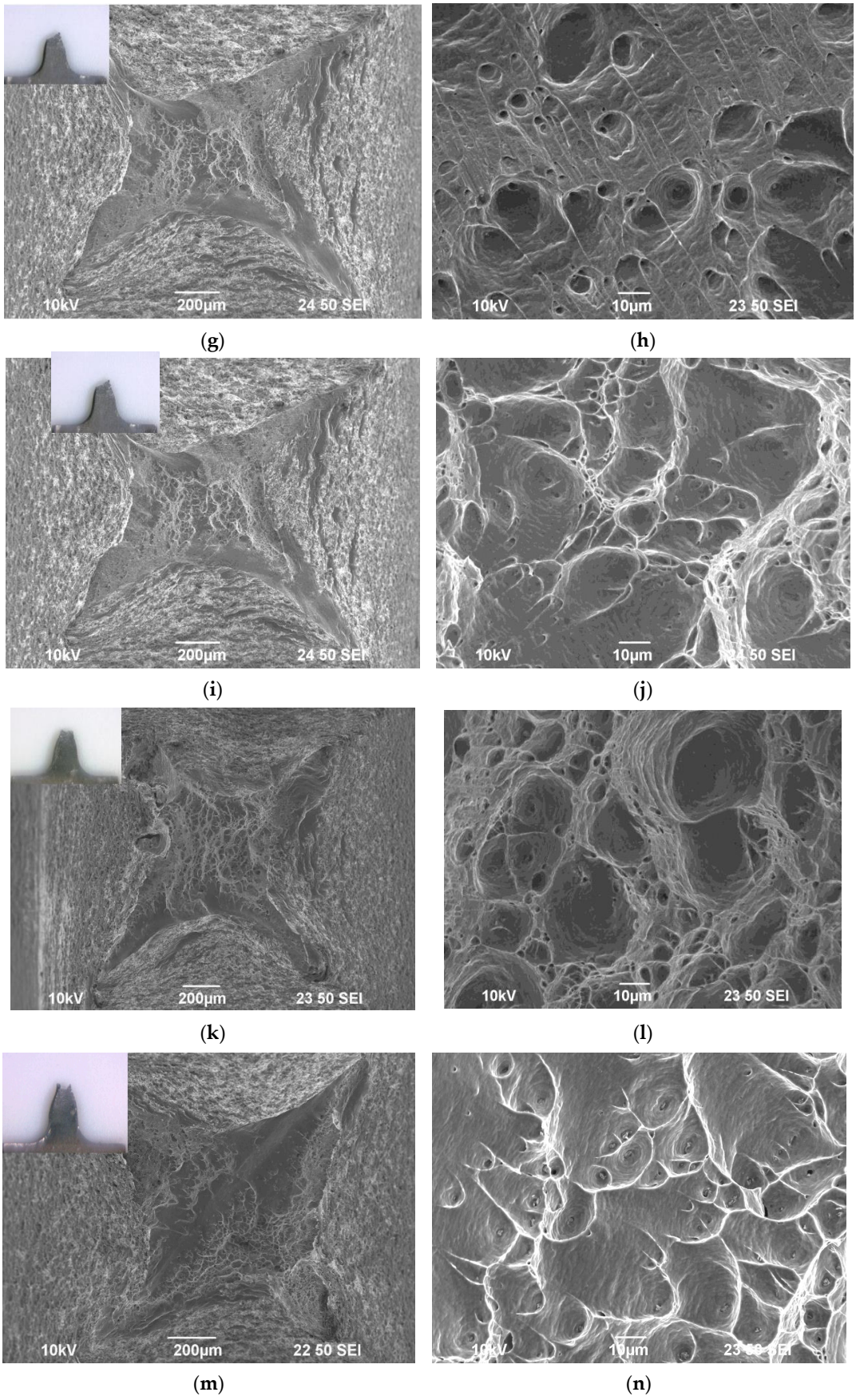
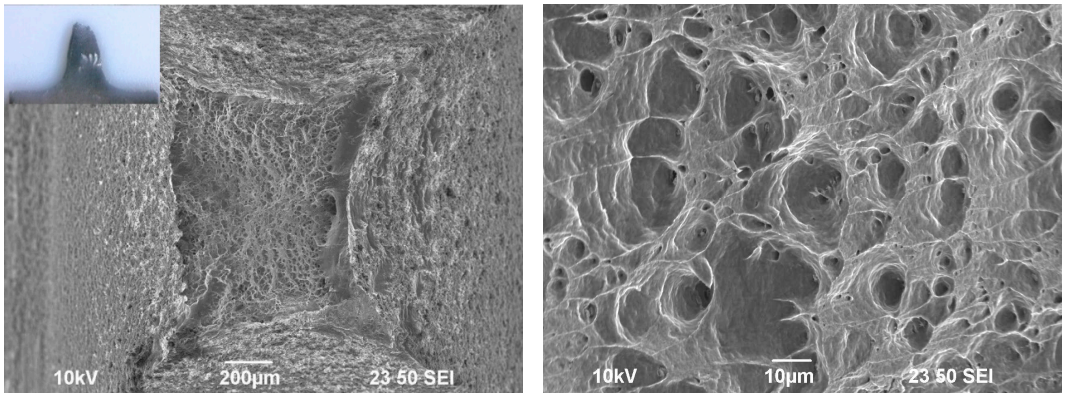


Figure A1. *Cont.*



(**o**) (**p**)

Figure A1. SEM images of the surface of fractures in alloy specimens No. 1 (**a**,**b**), 2 (**c**,**d**), 3 (**e**,**f**), 4 (**g**,**h**), 5 (**i**,**j**), **6** (**k**,**l**), 7 (**m**,**n**), and 8 (**o**,**p**) after tensile tests at room temperature.

Appendix B

Appendix B shows the stress–strain curves for the UFG alloy specimens tested at elevated temperatures and at a strain rate of 3.3×10^{-3} s^{-1}.

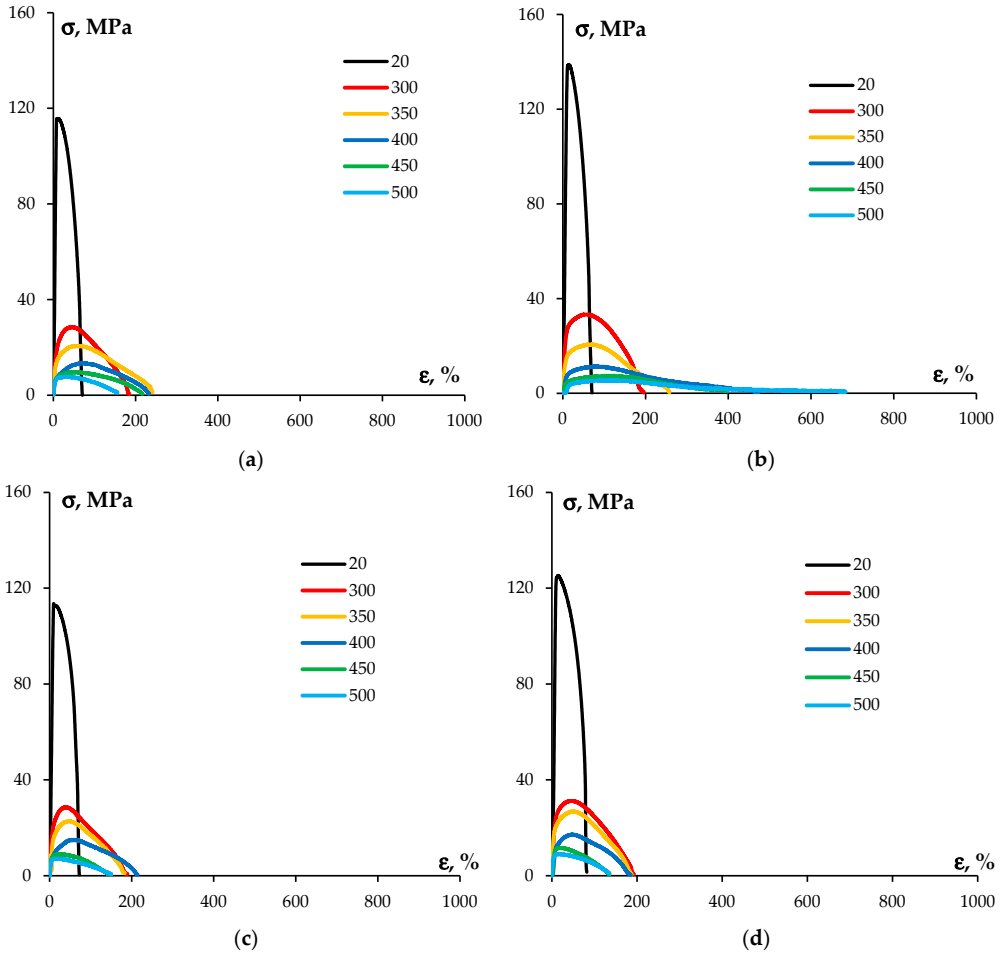


Figure A2. *Cont.*

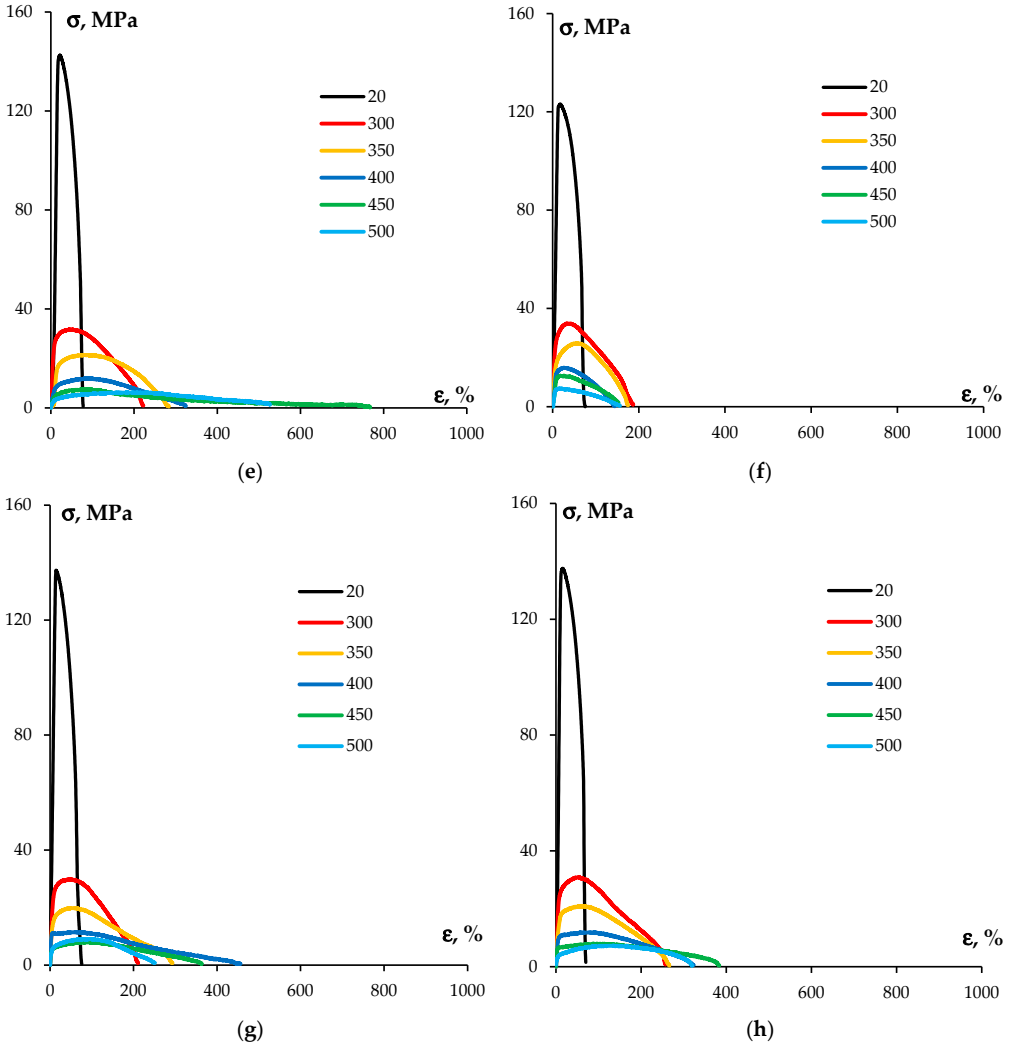


Figure A2. σ(ε) curves in UFG alloys series No. 1 (**a**), 2 (**b**), 3 (**c**), 4 (**d**), 5 (**e**), 6 (**f**), 7 (**g**), and 8 (**h**). Tests at elevated temperatures and a strain rate of 3.3×10^{-3} s^{-1}. Test temperatures are provided in the figures.

Appendix C

Appendix C shows the σ(ε) curves for the specimens deformed at different temperatures and at a strain rate of 3.3×10^{-3} s^{-1}.

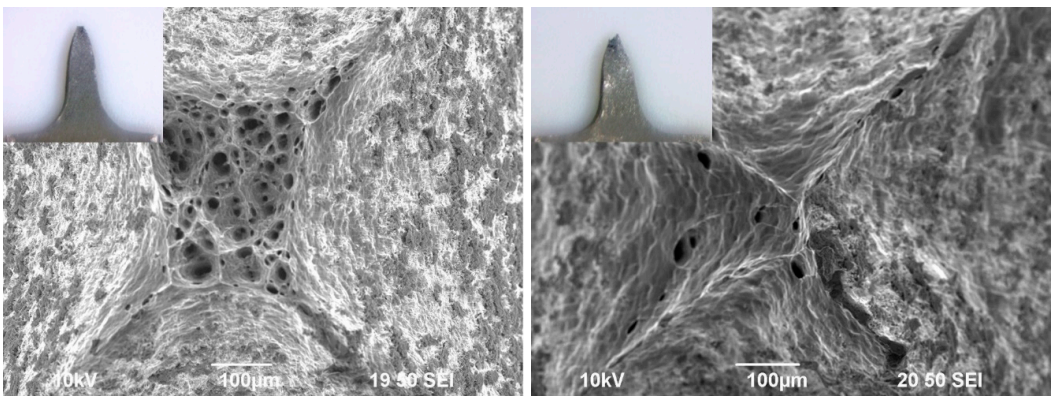
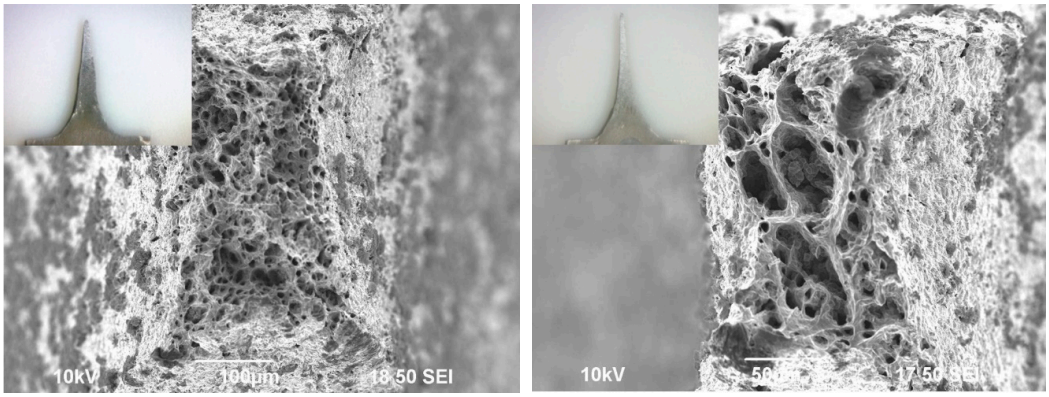
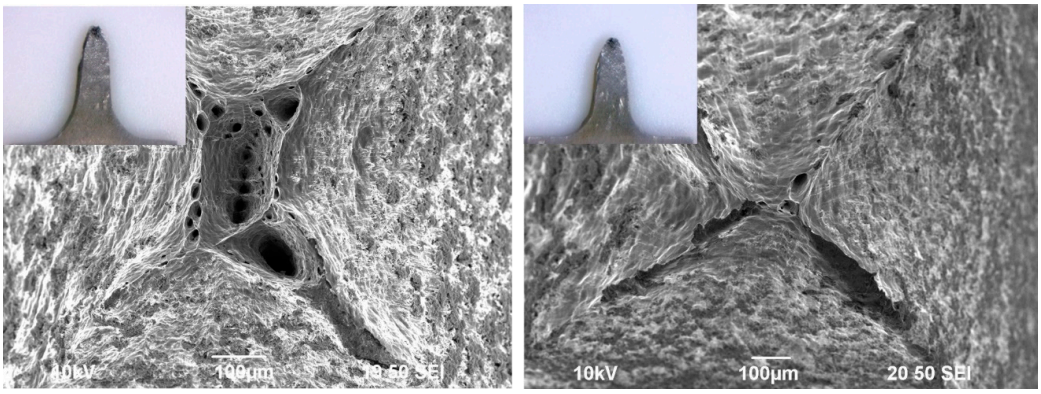


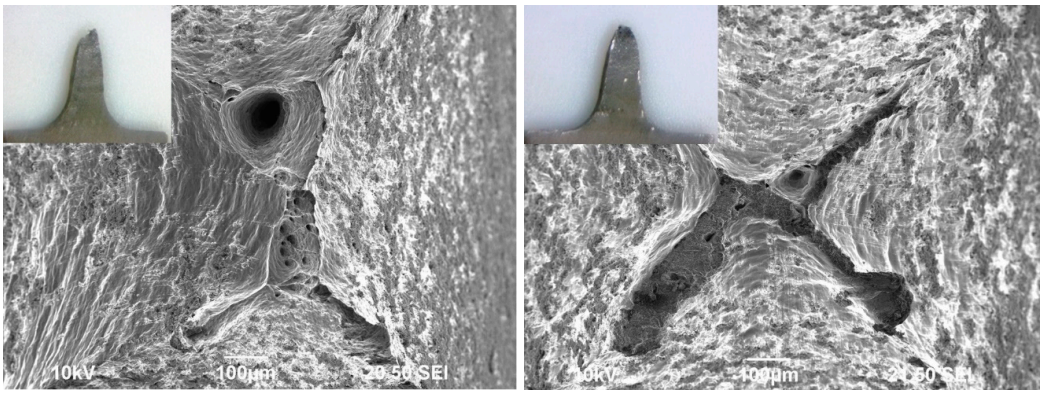
Figure A3. *Cont.*



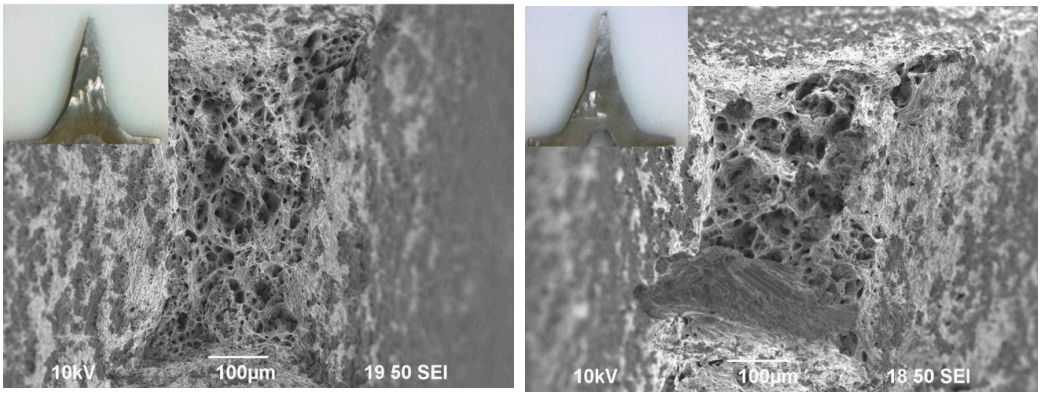
(**a2**) (**b2**)



(**a3**) (**b3**)

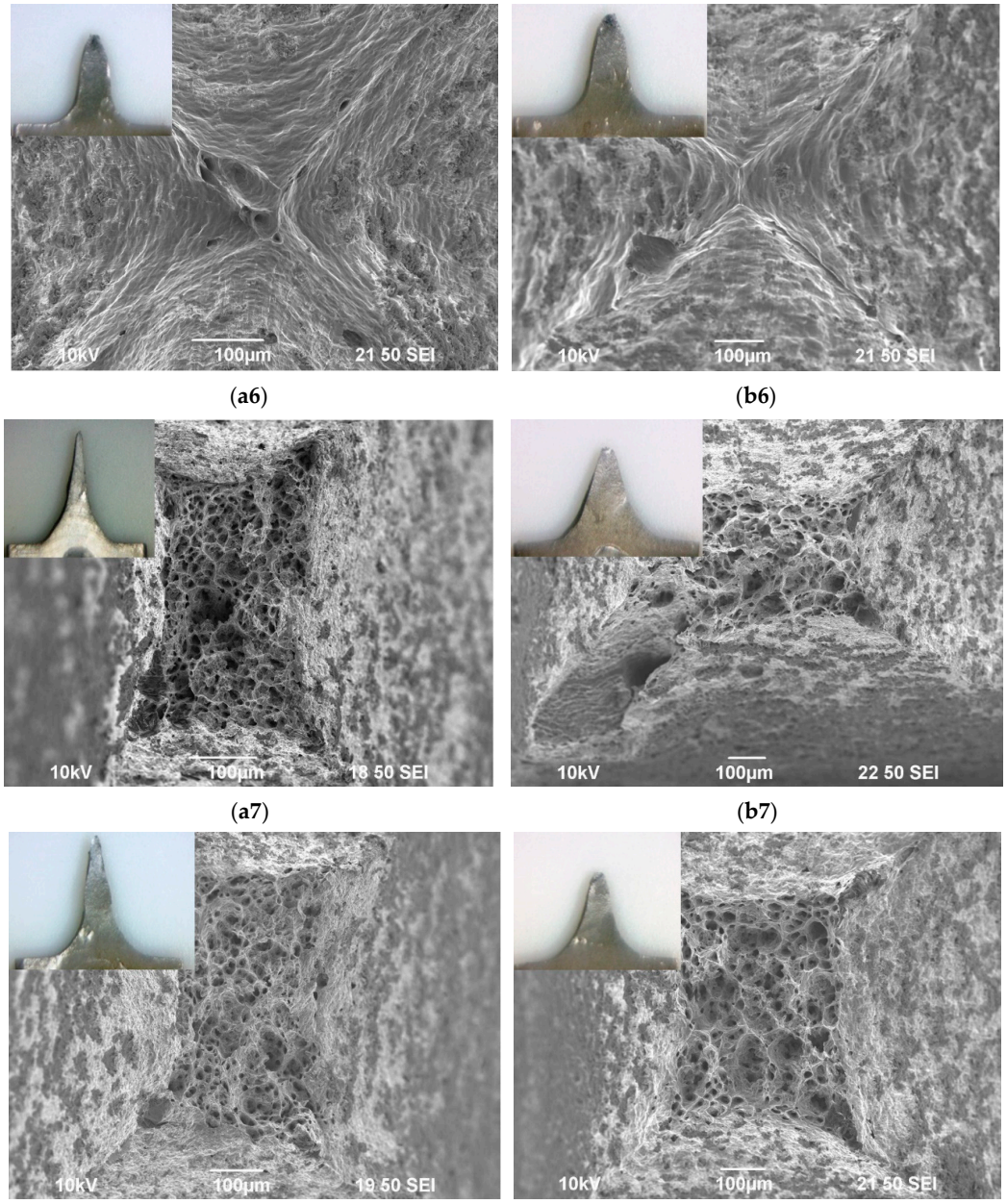


(**a4**) (**b4**)



(**a5**) (**b5**)

Figure A3. *Cont*.

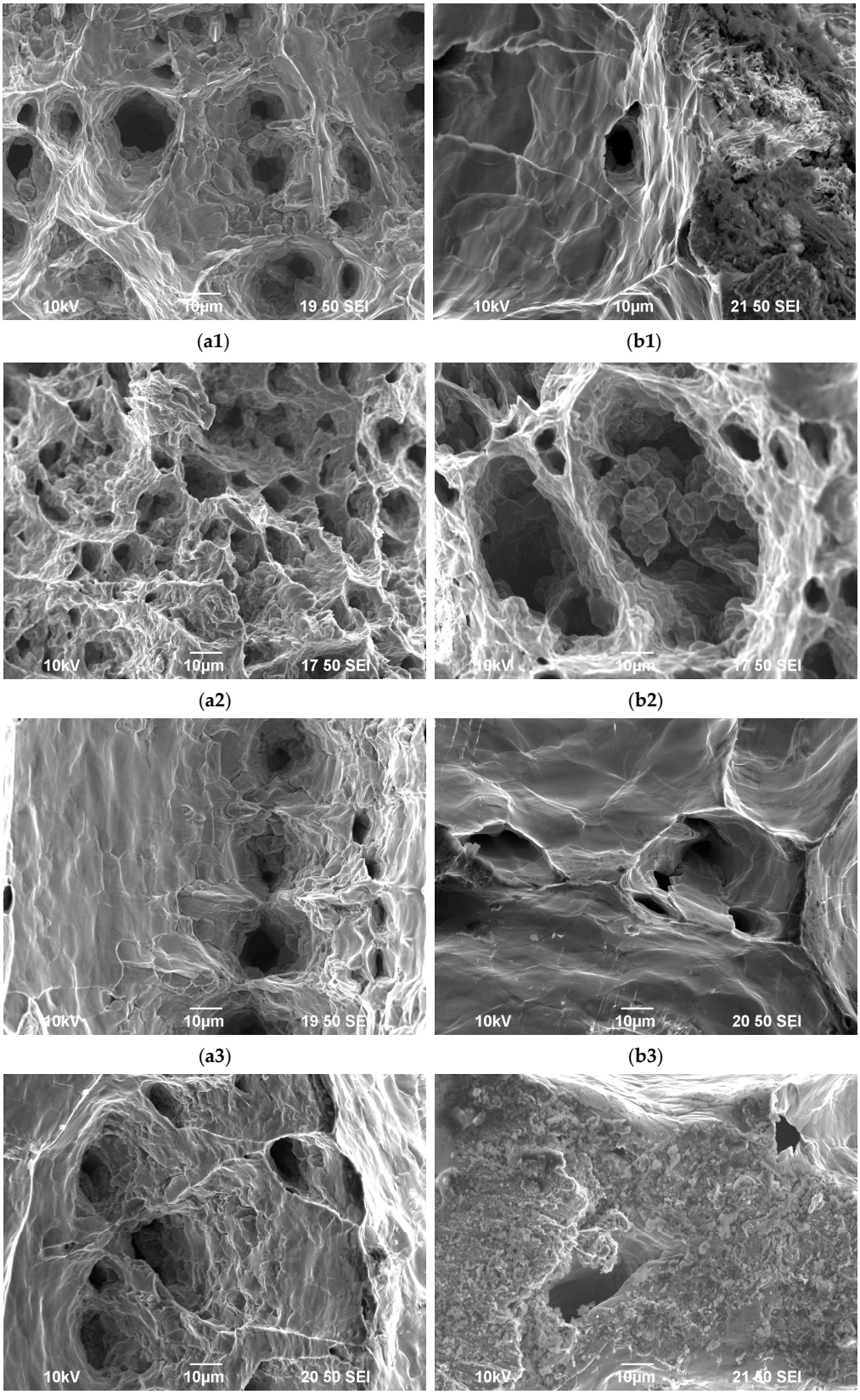


(**a6**) (**b6**)

(**a7**) (**b7**)

(**a8**) (**b8**)

Figure A3. General view of fractures in UFG alloy specimens No. 1 (**a1**,**b1**), 2 (**a2**,**b2**), 3 (**a3**,**b3**), 4 (**a4**,**b4**), 5 (**a5**,**b5**), 6 (**a6**,**b6**), 7 (**a7**,**b7**), and 8 (**a8**,**b8**) after tensile tests at 400 °C (**a1**–**a8**) and 500 °C (**b1**–**b8**). Strain rate of 3.3×10^{-3} s^{-1}.



(**a1**) (**b1**)

(**a2**) (**b2**)

(**a3**) (**b3**)

(**a4**) (**b4**)

Figure A4. *Cont*.

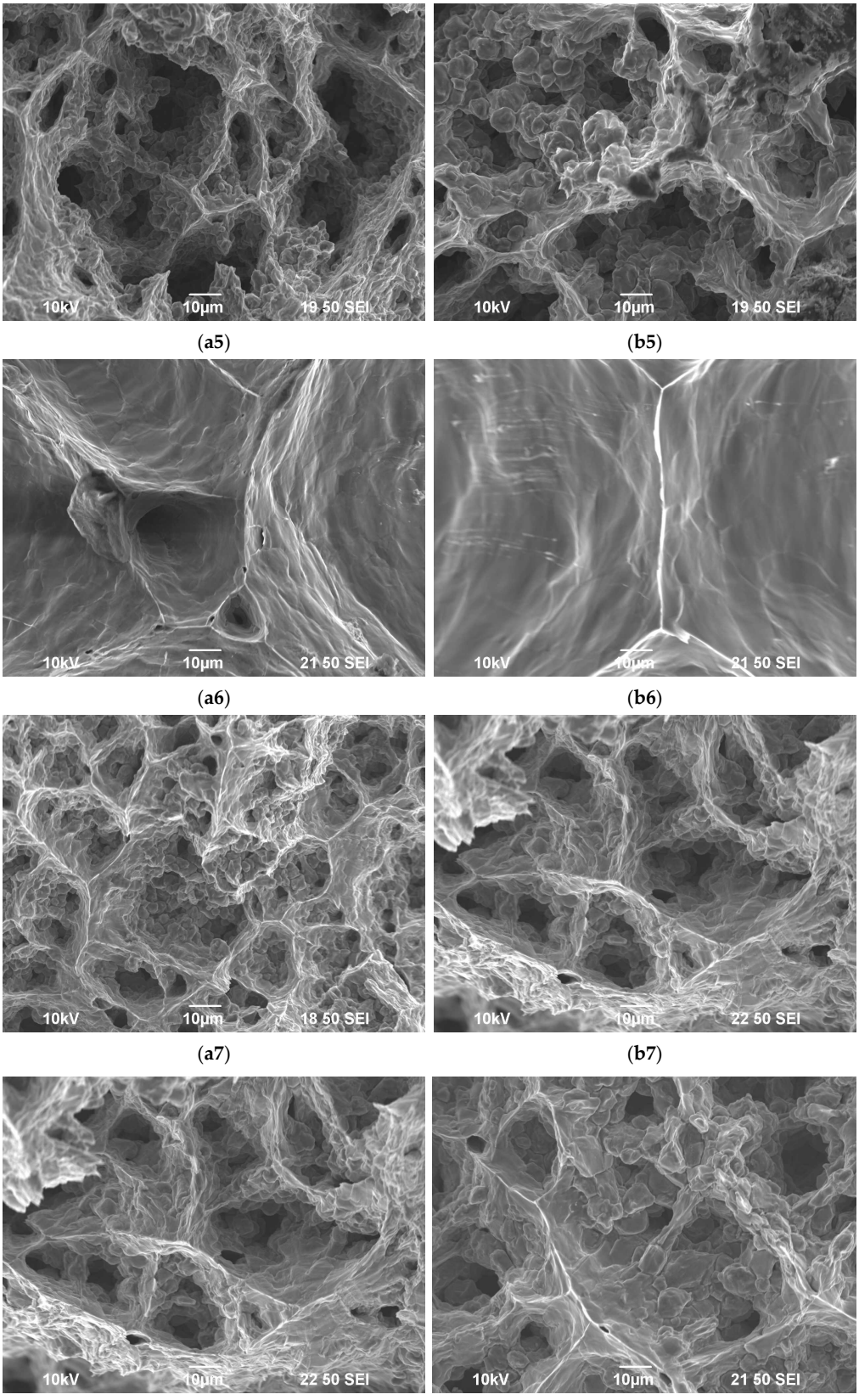


Figure A4. Central part of fractures in UFG alloy specimens No. 1 (**a1**,**b1**), 2 (**a2**,**b2**), 3 (**a3**,**b3**), 4 (**a4**,**b4**), 5 (**a5**,**b5**), 6 (**a6**,**b6**), 7 (**a7**,**b7**), and 8 (**a8**,**b8**) after tensile tests at 400 °C (**a1**–**a8**) and 500 °C (**b1**–**b8**). Strain rate of 3.3×10^{-3} s^{-1}.

References

1. Matveev, Y.A.; Gavrilova, V.P.; Baranov, V.V. Light conducting materials for aircraft wires. *Cables Wires* **2006**, *5*, 22–23. (In Russian)
2. Medvedev, A.; Arutyunyan, A.; Lomakin, I.; Bondarenko, A.; Kazykhanov, V.; Enikeev, N.; Raab, G.; Murashkin, M. Fatigue properties of ulta-fine grained Al-Mg-Si wires with enhanced mechanical strength and electrical conductivity. *Metals* **2018**, *8*, 1034. [CrossRef]
3. Li, Y.; Hu, A.; Fu, Y.; Liu, S.; Shen, W.; Hu, H.; Nie, X. Al alloys and casting processes for induction motor applications in battery-powered electric vehicles: A review. *Metals* **2022**, *12*, 216. [CrossRef]
4. Li, R.; Liu, H.; Ma, H.; Hou, J.; Qian, L.; Wang, Q.; Li, X.; Zhang, Z. Role of multi-scale microstructure in the degradation of Al wire for power transmission. *Appl. Sci.* **2020**, *10*, 2234. [CrossRef]
5. Shakirov, R.G.; Sattarov, R.R.; Gunderov, D.V.; Murashkin, M.Y. Evaluation of advanced aluminum alloys for use in new-generation wires. *Power Technol. Eng.* **2021**, *54*, 923–928. [CrossRef]
6. Yang, C.; Masquellier, N.; Gandiolle, C.; Sauvage, X. Multifunctional properties of composition graded Al wires. *Scr. Mater.* **2020**, *189*, 21–24. [CrossRef]
7. Teleshov, V.V.; Zakharov, V.V.; Zapolskaya, V.V. Development of aluminium alloys for high-temperature wires with enhanced strength and high specific electrical conduction. *Light Alloy. Technol.* **2018**, *1*, 15–26. (In Russian)
8. Belov, N.A.; Alabin, A.N.; Teleuova, A.R. Comparative analysis of alloying additives as applied to the production of heat-resistant aluminum-base wires. *Met. Sci. Heat Treat.* **2012**, *53*, 455–459. [CrossRef]
9. Korotkova, N.O.; Belov, N.A.; Timofeef, V.N.; Motkov, M.M.; Cherkasov, S.O. Influence of heat treatment on the structure and properties of an Al-7%REM conductive aluminum alloy casted in an electromagnetic crystallizer. *Phys. Met. Metallogr.* **2020**, *121*, 173–179. [CrossRef]
10. Mogucheva, A.A.; Zyabkin, D.V.; Kaibyshev, R.O. Effect of annealing on the structure and properties of aluminum alloy Al-8%MM. *Met. Sci. Heat Treat.* **2012**, *53*, 450–454. [CrossRef]
11. Murashkin, M.Y.; Sabirov, I.; Medvedev, A.E.; Enikeev, N.A.; Lefebvre, W.; Valiev, R.Z.; Sauvage, X. Mechanical and electrical properties of an ultrafine grained Al-8.5wt.%RE (RE = 5.4wt.%Ce, 3.1wt.%La) alloy processed by severe plastic deformation. *Mater. Des.* **2016**, *90*, 433–442. [CrossRef]
12. Medvedev, A.E.; Murashkin, M.Y.; Enikeev, N.A.; Valiev, R.Z.; Hodgson, P.D.; Lapovok, R. Enhancement of mechanical and electrical properties of Al-Re alloys by optimizing rare-earth concentration and thermo-mechanical treatment. *J. Alloys Compd.* **2018**, *745*, 696–704. [CrossRef]
13. Wang, W.; Pan, Q.; Lin, G.; Wang, X.; Sun, Y.; Wang, X.; Ye, J.; Sun, Y.; Yu, Y.; Jiang, F.; et al. Microstructure and properties of novel Al-Ce-Sc, Al-Ce-Y, Al-Ce-Zr and Al-Ce-Sc-Y alloy conductors processed by die casting, hot extrusion and cold drawing. *J. Mater. Sci. Technol.* **2020**, *58*, 155–170. [CrossRef]
14. Sidelnikov, S.B.; Voroshilov, D.S.; Motkov, M.M.; Timofeev, V.N.; Konstantinov, I.L.; Doyzhenko, N.N.; Lopatina, E.S.; Bespalov, V.M.; Sokolov, R.E.; Mansurov, Y.N.; et al. Investigation structure and properties of wire from the alloy of Al-REM system obtained with the application of casting in the electromagnetic mold, combined rolling-extrusion, and drawing. *Int. J. Adv. Manuf. Technol.* **2021**, *114*, 2633–2649. [CrossRef]
15. Zakharov, V.V. Prospects of creation of aluminum alloys sparingly alloyed with scandium. *Met. Sci. Heat Treat.* **2018**, *60*, 172–176. [CrossRef]
16. Zakharov, V.V. Stability of the solid solution of scandium in aluminum. *Met. Sci. Heat Treat.* **1997**, *39*, 61–66. [CrossRef]
17. Zakharov, V.V. Cobmined alloying of aluminum alloys with scandium and zirconium. *Met. Sci. Heat Treat.* **2014**, *56*, 281–286. [CrossRef]
18. Røyset, J.; Ryum, N. Scandium in aluminum alloys. *Int. Mater. Rev.* **2005**, *50*, 19–44. [CrossRef]
19. Filatov, Y.A.; Elagin, V.I.; Zakharov, V.V. New Al-Mg-Sc alloys. *Mater. Sci. Eng. A* **2000**, *280*, 97–101. [CrossRef]
20. Toropova, L.S.; Eskin, D.G.; Kharakterova, M.L.; Dobatkina, T.V. *Advanced Aluminum Alloys Containing Scandium*; Taylor and Francis: London, UK, 2017; 175p.
21. Davydov, V.G.; Rostova, T.D.; Zakharov, V.V.; Filatov, Y.A.; Yelagin, V.I. Scientific principles of making an alloying of scandium to aluminium alloys. *Mater. Sci. Eng. A* **2000**, *280*, 30–36. [CrossRef]
22. Eskin, D.G. Sc applications in aluminum alloys: Overview of Russian research in the 20th century. *Miner. Met. Mater. Ser.* **2018**, *F4*, 1565–1572. [CrossRef]
23. Eskin, D.G. The scandium story–Part II: Impact on aluminum alloys and their applications. *Light Met. Age* **2020**, *78*, 40–44.
24. Latynina, T.A.; Mavlyutov, A.M.; Valiev, R.Z.; Murashkin, M.Y.; Orlova, T.S. The effect of hardening by annealing in ultrafine-grained Al-0.4Zr alloy: Influence of Zr microadditives. *Philos. Mag.* **2019**, *99*, 2424–2443. [CrossRef]
25. Belov, N.; Korotkova, N.; Akopyan, T.; Murashkin, M.; Timofeev, V. Structure and properties of Al-0.6wt.%Zr wire alloy manufactured by direct drawing of electromagnetically cast wire rod. *Metals* **2020**, *10*, 769. [CrossRef]
26. Mohammadi, A.; Enikeev, N.A.; Murashkin, M.Y.; Arita, M.; Edalati, K. Developing age-hardenable Al-Zr alloy by ultra-severe plastic deformation: Significance of supersaturation, segregation and precipitation on hardening and electrical conductivity. *Acta Mater.* **2021**, *203*, 116503. [CrossRef]
27. Orlova, T.S.; Latynina, T.A.; Mavlyutov, A.M.; Murashkin, M.Y.; Valev, R.Z. Effect of annealing on microstructure, strength and electrical conductivity of the pre-aged and HPT-processed Al-0.4Zr alloy. *J. Alloys Compd.* **2019**, *784*, 41–48. [CrossRef]

28. Belov, N.A.; Alabin, A.N.; Yakovlev, A.A. Influence of the annealing temperature on the phase composition of Al-0.55 wt%Zr cast alloy. *Russ. J. Non-Ferr. Met.* **2013**, *54*, 224–228. [CrossRef]
29. Belov, N.A.; Korotkova, N.O.; Akopyan, T.K.; Timofeev, V.N. Structure and properties of Al-0.6%Zr-0.4%Fe-0.4%Si (wt.%) wire alloy manufactured by electromagnetic casting. *JOM* **2020**, *72*, 1561–1570. [CrossRef]
30. Lefebre, W.; Skiba, N.V.; Chabanais, F.; Gutkin, M.Y.; Rigutti, L.; Murashkin, M.Y.; Orlova, T.S. Vacancy release upon heating of an ultrafine grain Al-Zr alloy: In-situ observations and theoretical modeling. *J. Alloys Compd.* **2021**, *862*, 158455. [CrossRef]
31. Orlova, T.S.; Mavlyutov, A.M.; Latynina, T.A.; Ubyivovk, E.V.; Murashkin, M.M.; Schneider, R.; Gerthsen, D.; Valiev, R.Z. Influence of severe plastic deformation on microstructure, strength and electrical conductivity of aged Al-0.4Zr (wt.%) alloy. *Rev. Adv. Mater. Sci.* **2018**, *55*, 92–101. [CrossRef]
32. Fuller, C.B.; Murray, J.L.; Seidman, D.N. Temporal evolution of the nanostructure of Al(Sc,Zr) alloys: Part I–Chemical compositions of $Al_3(Sc_{1-x}Zr_x)$ precipitates. *Acta Mater.* **2005**, *53*, 5401–5413. [CrossRef]
33. Terumi, M.; Shinichiro, F.; Ken-ichi, H. Duffusion of zirconium in aluminum. *J. Jpn. Inst. Light Met.* **1973**, *23*, 17–25. [CrossRef]
34. Knipling, K.E.; Dunand, D.C.; Seidman, D.N. Precipitation evolution in Al-Zr and Al-Zr-Ti alloys during aging at 450–600 °C. *Acta Mater.* **2008**, *56*, 1182–1195. [CrossRef]
35. Nes, E.; Ryum, N. On the formation of fan-shaped precipitates during the decomposition of a highly supersaturated Al-Zr solid solution. *Scr. Mater.* **1971**, *5*, 987–989. [CrossRef]
36. Nes, E.; Billdal, H. The mechanism of discontinuous precipitation of the metastable Al_3Zr phase from an Al-Zr solid solution. *Acta Metall.* **1977**, *25*, 1039–1046. [CrossRef]
37. Mikhaylovskaya, A.V.; Mochugovskiy, A.G.; Levchenko, V.S.; Tabachkova, N.Y.; Mufalo, W.; Portnoy, V.K. Precipitation behavior of $L1_2$ Al_3Zr phase in Al-Mg-Zr alloy. *Mater. Charat.* **2018**, *139*, 30–37. [CrossRef]
38. Mochugovskiy, A.G.; Mikhaylovskaya, A.V. Comparison of precipitation kinetics and mechanical properties in Zr and Sc-bearing aluminum-based alloys. *Mater. Lett.* **2020**, *275*, 128096. [CrossRef]
39. Mochugovskiy, A.G.; Mikhaylovskaya, A.V.; Zadorognyy, M.Y.; Golovin, I.S. Effect of heat treatment on the grain size control, superplasticity, internal friction, and mechanical properties of zirconium-bearing aluminum-based alloy. *J. Alloys Compd.* **2021**, *856*, 157455. [CrossRef]
40. Pozdnyakov, A.V.; Osipenkova, A.A.; Popov, D.A.; Makhov, S.V.; Napalkov, V.I. Effect of low additions of Y, Sm, Gd, Hf and Er on the structure and hardness of alloy Al-0.2%Zr-0.1%Sc. *Met. Sci. Heat Treat.* **2017**, *58*, 537–542. [CrossRef]
41. Wen, S.P.; Gao, K.Y.; Huang, H.; Wang, W.; Nie, Z.R. Role of Yb and Si on the precipitation hardening and recrystallization of dilute Al-Zr alloy. *J. Alloys Compd.* **2014**, *599*, 65–70. [CrossRef]
42. Wen, S.P.; Gao, K.Y.; Li, Y.; Huang, H.; Nie, Z.R. Synergetic effect of Er and Zr on the precipitation hardening of Al-Er-Zr alloy. *Scr. Mater.* **2011**, *65*, 592–595. [CrossRef]
43. Voroshilov, D.S.; Motkov, M.M.; Sidelnikov, S.B.; Sokolov, S.E.; Durnopyanov, A.V.; Konstantinov, I.L.; Bespalov, V.M.; Bermeshev, T.V.; Gudkov, I.S.; Voroshilova, M.V.; et al. Obtaining Al-Zr-Hf wire using electromagnetic casting, combined rolling-extrusion, and drawing. *Int. J. Lightweight Mater. Manuf.* **2022**, *5*, 352–368. [CrossRef]
44. Zhou, T.; Xie, H.; Jiang, Z. Mechanical and electrical properties of Y-containing Al-Zr heat-resistant alloy produced by dynamic ECAE process. *J. Wuhan Univ. Techn.* **2022**, *37*, 123–129. [CrossRef]
45. Knipling, K.E.; Seidman, D.N.; Dunand, D.C. Ambient- and high-temperature mechanical properties of isochronally aged Al-0.06Sc, Al-0.06Zr and Al-0.06Sc-0.06Zr (at.%) alloys. *Acta Mater.* **2011**, *59*, 943–954. [CrossRef]
46. Li, H.; Bin, J.; Liu, J.; Gao, Z.; Lu, X. Precipitation evolution and coarsening resistance at 400 °C of Al microalloyed with Zr and Er. *Scr. Mater.* **2012**, *67*, 73–76. [CrossRef]
47. Kang, W.; Li, H.Y.; Zhao, S.X.; Han, Y.; Yang, C.L.; Ma, G. Effects of homogenization treatments on the microstructure evolution, microhardness and electrical conductivity of dilute Al-Sc-Zr-Er alloys. *J. Alloys Compd.* **2017**, *704*, 683–692. [CrossRef]
48. Luca, A.D.; Dunand, D.C.; Seidman, D.N. Microstructure and mechanical properties of a precipitation-strengthened Al-Zr-Sc-Er-Si alloy with a very small Sc content. *Acta Mater.* **2018**, *144*, 80–91. [CrossRef]
49. Mochegovskiy, A.G.; Mikhaylovskaya, A.V.; Tabachkova, N.Y.; Portnoy, V.K. The mechanism of $L1_2$ precipitation, microstructure and tensile properties of Al-Mg-Er-Zr alloy. *Mater. Sci. Eng. A* **2019**, *744*, 195–205. [CrossRef]
50. Cao, F.; Teng, X.; Su, R.; Liang, J.; Liu, R.; Kong, S.; Guo, N. Room temperature strengthening mechanisms, high temperature deformation behavior and constitutive modeling in an Al-3.25Mg-0.37Zr-0.28Mn-0.19Y alloy. *J. Mater. Res. Technol.* **2022**, *18*, 962–977. [CrossRef]
51. Gao, Z.; Li, H.; Liu, J.; Lu, X.; Ou, Y. Effects of ytterbium and zirconium on precipitation evolution and coarsening resistance in aluminum during isothermal aging. *J. Alloys Compd.* **2014**, *592*, 100–104. [CrossRef]
52. Wu, H.; Wen, S.P.; Wu, X.L.; Gao, K.Y.; Huang, H.; Wang, W.; Nie, Z.R. A study of precipitation strengthening and recrystallization behavior in dilute Al-Er-Hf-Zr alloys. *Mater. Sci. Eng. A* **2015**, *639*, 307–313. [CrossRef]
53. Gao, H.; Feng, W.; Gu, J.; Wang, J.; Sun, B. Aging and recrystallization behavior of precipitation strengthened Al-0.25Zr-0.03Y alloy. *J. Alloys Compd.* **2017**, *696*, 1039–1045. [CrossRef]
54. Li, H.; Gao, Z.; Yin, H.; Jiang, H.; Su, X.; Bin, J. Effects of Er and Zr additions on precipitation and recrystallization of pure aluminum. *Scr. Mater.* **2013**, *68*, 59–62. [CrossRef]
55. Wen, S.P.; Wang, W.; Zhao, W.H.; Wu, X.L.; Gao, K.Y.; Huang, H.; Nie, Z.R. Precipitation hardening and recrystallization behavior of Al-Mg-Er-Zr alloys. *J. Alloys Compd.* **2016**, *687*, 143–151. [CrossRef]

56. Zhang, Y.; Zhou, W.; Gao, H.; Han, Y.; Wang, K.; Wang, J.; Sun, B.; Gu, S.; You, W. Precipitation evolution of Al-Zr-Yb alloys during isochronal aging. *Scr. Mater.* **2013**, *69*, 477–480. [CrossRef]
57. Mochegovskiy, A.G.; Barkov, R.Y.; Mikhaylovskaya, A.V.; Loginova, L.S.; Yakovtseva, O.A.; Pozdniakov, A.V. Structure and properties of Al-4.5Mg-0.15Zr compositions alloyed with Er, Y, and Yb. *Phys. Met. Metallogr.* **2022**, *123*, 466–473. [CrossRef]
58. Gao, H.; Wang, Y.; Wang, J.; Sun, B.; Apelian, D. Aging and recrystallization behavior of quaternary Al-0.25Zr-0.03Y-0.10Si alloy. *Mater. Sci. Eng. A* **2019**, *763*, 138160. [CrossRef]
59. Wen, S.P.; Gao, K.Y.; Huang, H.; Wang, W.; Nie, Z.R. Precipitation evolution in Al-Er-Zr alloys during aging at elevated temperature. *J. Alloys Compd.* **2013**, *574*, 92–97. [CrossRef]
60. Farkoosh, A.R.; Dunand, D.C.; Seidman, D.N. Effects of W and Si microadditions on microstructure and the strength of dilute precipitation-strengthened Al-Zr-Er alloys. *Mater. Sci. Eng. A* **2020**, *798*, 140159. [CrossRef]
61. Pozdniakov, A.V.; Barkov, R.Y.; Prosviryakov, A.S.; Churyumov, A.Y.; Golovin, I.S.; Zolotorevskiy, V.S. Effect of Zr on the microstructure, recrystallization behavior, mechanical properties and electrical conductivity of the novel Al-Er-Y alloy. *J. Alloys Compd.* **2018**, *765*, 1–6. [CrossRef]
62. Zhang, Y.; Gao, H.; Kuai, Y.; Han, Y.; Wang, J.; Sun, B.; Gu, S.; You, W. Effects of Y additions on the precipitation and recrystallization of Al-Zr alloys. *Mater. Charat.* **2013**, *86*, 1–8. [CrossRef]
63. Wu, H.; Zhang, Q.; Li, L.; Huang, M.; Zheng, Z.; Wen, S. Thermal stability of the precipitates in dilute Al-Er-Zr/Hf alloys at elevated temperatures. *Metals* **2022**, *12*, 1242. [CrossRef]
64. Michi, R.A.; Luca, A.D.; Seidman, D.N.; Dunand, D.C. Effects of Si and Fe micro-additions on the aging response of a dilute Al-0.08Zr-0.08Hf-0.045Er at.% alloy. *Mater. Charact.* **2019**, *147*, 72–83. [CrossRef]
65. Leibner, M.; Vlach, M.; Kodetová, V.; Kudrnová, H.; Veselý, J.; Zikmund, S.; Čížek, J.; Melikhova, O.; Lukáč, F. Effect of deformation o evolution of Al_3(Er,Zr) precipitates in Al-Er-Zr-based alloy. *Mater. Charact.* **2022**, *186*, 111781. [CrossRef]
66. Schmid, F.; Gehringer, D.; Kremmer, T.; Cattini, L.; Uggowitzer, P.J.; Holec, D.; Pogatscher, S. Stabilization of Al_3Zr allotropes in dilute aluminum alloys via the addition of ternary elements. *Materialia* **2022**, *21*, 101321. [CrossRef]
67. Nokhrin, A.; Shadrina, I.; Chuvil'deev, V.; Kopylov, V. Study of structure and mechanical properties of fine-grained aluminum alloys Al-0.6wt.%Mg-Zr-Sc with ratio Zr:Sc = 1.5 obtained by cold drawing. *Materials* **2019**, *12*, 316. [CrossRef]
68. Nokhrin, A.V.; Shadrina, I.S.; Chuvil'deev, V.N.; Kopylov, V.I.; Berendeev, N.N.; Murashov, A.A.; Bobrov, A.A.; Tabachkova, N.Y.; Smirnova, E.S.; Faddeev, M.A. Investigation of thermal stability of microstructure and mechanical properties of bimetallic fine–grained wires from Al–0.25%Zr–(Sc,Hf) alloys. *Materials* **2022**, *15*, 185. [CrossRef]
69. Bobruk, E.A.; Safargalina, Z.A.; Golubev, O.V.; Baykov, D.; Kazykhanov, V.U. The effect of ultrafine-grained states on superplastic behavior of Al-Mg-Si alloy. *Mater. Lett.* **2019**, *255*, 126503. [CrossRef]
70. Chayoumabadi, M.E.; Mochugovskiy, A.G.; Tabachkova, N.Y.; Mikhaylovskaya, A.V. The influence of minor additions of Y, Sc, and Zr on the microstructural evolution, superplastic behavior, and mechanical properties of AA6013 alloy. *J. Alloys Compd.* **2022**, *900*, 163477. [CrossRef]
71. Mochugovskiy, A.G.; Prosviryakov, A.S.; Tabachkova, N.Y.; Mikhaylovskaya, A.V. The effect of Ce on the microstructure, superplasticity, and mechanical properties of Al-Mg-Si-Cu alloy. *Metals* **2022**, *12*, 512. [CrossRef]
72. Mikhaylovskaya, A.V.; Chayoumabadi, M.E.; Mochugovskiy, A.G. Superplasticity and mechanical properties of Al-Mg-Si alloy doped with eutectic-forming Ni and Fe, and dispesoid-forming Sc and Zr elements. *Mater. Sci. Eng. A* **2021**, *817*, 141319. [CrossRef]
73. Bobruk, E.V.; Dolzhenko, P.D.; Murashkin, M.Y.; Valiev, R.Z.; Enikeev, N.A. The microstructure and strength of UFG 6060 alloy after superplastic deformation at a lower homologous temperature. *Materials* **2022**, *15*, 6983. [CrossRef] [PubMed]
74. Jafarian, H.R.; Anijdan, S.H.M.; Miyamoto, H. Observations of low temperature superplasticity in an ultrafine grained AA6063 alloy. *Mater. Sci. Eng. A* **2020**, *795*, 140015. [CrossRef]
75. Troeger, L.P.; Starke, E.A., Jr. Microstructural and mechanical characterization of a superplastic 6xxx aluminum alloy. *Mater. Sci. Eng. A* **2000**, *277*, 102–113. [CrossRef]
76. Mochugovskiy, A.; Kotov, A.; Chayoumabadi, M.E.; Yakovtseva, O.; Mikhaylovskaya, A. A high-strain-rate superplasticity of the Al-Mg-Si-Zr-Sc alloy with Ni addition. *Materials* **2021**, *14*, 2028. [CrossRef] [PubMed]
77. Kim, W.J.; Kim, J.K.; Park, T.Y.; Hong, S.I.; Kim, D.I.; Kim, Y.S.; Lee, J.D. Enhancement of strength and superplasticity in a 6061 Al alloy processed by equal-channel-angular-pressing. *Metall. Mater. Trans. A* **2002**, *33*, 3155–3164. [CrossRef]
78. Khamei, A.A.; Dehghani, K. Effects of strain rate and temperature on hot tensile deformation of severe plastic deformed 6061 aluminum alloy. *Mater. Sci. Eng. A* **2015**, *627*, 1–9. [CrossRef]
79. Katsas, S.; Dashwood, R.; Grimes, R.; Jackson, M.; Todd, G.; Henein, H. Dynamic recrystallization and superplasticity in pure aluminum with zirconium addition. *Mater. Sci. Eng. A* **2007**, *444*, 291–297. [CrossRef]
80. Chuvil'deev, V.N.; Gryaznov, M.Y.; Shotin, S.V.; Kopylov, V.I.; Nokhrin, A.V.; Likhnitskii, C.V.; Chegurov, M.K.; Bobrov, A.A.; Tabachkova, N.Y.; Pirozhnikova, O.E. Investigation of superplasticity and dynamic grain growth in ultrafine-grained Al-0.5%Mg-Sc alloys. *J. Alloys Compd.* **2021**, *877*, 160099. [CrossRef]
81. Gryaznov, M.Y.; Shotin, S.V.; Nokhrin, A.V.; Chuvil'deev, V.N.; Likhnitskii, C.C.; Kopylov, V.I.; Chegurov, M.K.; Shadrina, I.S.; Tabachkova, N.Y.; Smirnova, E.S.; et al. Investigation of effect of preliminary annealing on superplasticity of ultrafine-grained conductor aluminum alloys Al-0.5%Mg-Sc. *Materials* **2022**, *15*, 176. [CrossRef]

82. Kulifeev, V.K.; Stanolevich, G.P.; Kozlov, V.G. Aluminum-ytterbium phase diagram. *Izv. Vyssh. Ucheb. Zaved. Tsvet. Met.* **1971**, *4*, 108–110. (In Russian)
83. Paleznova, A. The ytterbium-aluminum system. *J. Less Comm. Met.* **1972**, *29*, 289–292. [CrossRef]
84. Meng, F.G.; Zhang, L.G.; Liu, H.S.; Liu, L.B.; Jin, Z.P. Thermodynamic optimization of the Al-Yb binary system. *J. Alloys Compd.* **2008**, *452*, 279–282. [CrossRef]
85. Gschneidner, K.A.; Calderwood, F.W. The Al-Yb (Aluminum-Ytterbium) system. *Bull. Alloy Phase Diagr.* **1989**, *10*, 47–79. [CrossRef]
86. Zhang, Y.; Gao, K.; Wen, S.; Huang, H.; Wang, W.; Zhu, Z.; Nie, Z.; Zhou, D. Determination of Er and Yb solvuses and trialuminide nucleation in Al-Er and Al-Yb alloys. *J. Alloys Compd.* **2014**, *590*, 526–534. [CrossRef]
87. Dalen, M.E.; Karnesky, R.A.; Cabotaje, J.R.; Dunand, D.C.; Seidman, D.N. Erbium and ytterbium solubilities and diffusivities in aluminum as determined by nanoscale characterization of precipitates. *Acta Mater.* **2009**, *57*, 4081–4089. [CrossRef]
88. Kodetová, V.; Vlach, M.; Bajtošová, L.; Leibner, M.; Kudrnová, H.; Málek, J.; Mára, V.; Cieslar, M.; Zikmund, S. Heat treatment of cast and cold rolled Al-Yb and Al-Mn-Yb-Zr alloys. *Materials* **2021**, *14*, 7122. [CrossRef]
89. Barkov, R.Y.; Yakovtseva, O.A.; Mamzurina, O.I.; Loginova, I.S.; Medvedeva, S.V.; Prosviryakov, A.S.; Mikhaylovskaya, A.V.; Pozdniakov, A.V. Effect of Yb on the structure and properties of an electroconductive Al-Y-Sc alloy. *Phys. Met. Metallogr.* **2020**, *121*, 604–609. [CrossRef]
90. Tang, C.-I.; Zhou, D.-J. Precipitation hardening behavior of dilute binary Al-Yb alloy. *Transact. Nonferr. Met. Soc. China* **2014**, *24*, 2326–2330. [CrossRef]
91. Van Dalen, M.E.; Gyger, T.; Dunand, D.C.; Seidman, D.N. Effects of Yb and Zr microalloying additions on the microstructure and mechanical properties of dilute Al-Sc alloys. *Acta Mater.* **2011**, *59*, 7615–7626. [CrossRef]
92. Karnesky, R.A.; van Dalen, M.E.; Dunand, D.C.; Seidman, D.N. Effects of substituting rare-earth elements for scandium in a precipitation-strengthened Al-0.08 at.%Sc alloy. *Scr. Mater.* **2006**, *55*, 437–440. [CrossRef]
93. Van Dalen, M.E.; Dunand, D.C.; Seidman, D.N. Microstructural evolution and creep properties of precipitation-strengthened Al-0.06Sc-0.02Gd and Al-0.06Sc-0.02Yb (at.%) alloys. *Acta Mater.* **2011**, *59*, 5224–5237. [CrossRef]
94. Sasaki, T.T.; Morris, R.A.; Thompson, G.B.; Syarif, Y.; Fox, D. Formation of ultra-fine copper grains in copper clad aluminum wire. *Scr. Mater.* **2010**, *63*, 488–491. [CrossRef]
95. Abbasi, M.; Taheri, A.K.; Salehi, M.T. Growth rate of intermetallic compounds in Al/Cu bimetal. *J. Alloy. Compd.* **2001**, *319*, 233–241. [CrossRef]
96. Gueydan, A.; Domengès, B.; Hug, E. Study of the intermetallic growth in copper-clad aluminum wires after thermal aging. *Intermetallics* **2014**, *50*, 34–42. [CrossRef]
97. Segal, V. Review: Modes and Processes of Severe Plastic Deformation. *Materials* **2018**, *11*, 1175. [CrossRef]
98. Segal, V.M.; Beyerlein, I.J.; Tome, C.N.; Chuvil'deev, V.N.; Kopylov, V.I. *Fundamentals and Engineering of Severe Plastic Deformation*; Nova Science Publishers: New York, NY, USA, 2010; 549p.
99. Boyer, H.E. *Metals Handbook. Fractography and Atlas of Fractographs*, 8th ed.; V. 9; American Society for Metals: William Park Woodside, OH, USA, 1974; 499p.
100. Nieh, T.G.; Wadsworth, J.; Sherby, O.D. *Superplasticity in Metals and Ceramics*; Cambridge University Press: Cambridge, UK, 1997; 288p.
101. Perevezentsev, V.N.; Rybin, V.V.; Chuvil'deev, V.N. The theory of structural superplasticity: IV. Cavitation during superplastic deformation. *Acta Metall. Mater.* **1992**, *40*, 915–923. [CrossRef]
102. Padmanabhan, K.A.; Engler, O.; Lücke, K. On the effects of second phase distribution on the fracture behaviour of two superplastic aluminum alloys. *J. Mater. Sci.* **1996**, *31*, 3971–3981. [CrossRef]
103. Chuvil'deev, V.N.; Gryaznov, M.Y.; Shotin, S.V.; Nokhrin, A.V.; Kopylov, V.I.; Chegurov, M.K.; Bobrov, A.A.; Shadrina, I.S.; Vostokov, M.M. Investigation of superplasticity of ultrafine-grained copper alloys obtained using ECAP. *J. Phys. Conf. Ser.* **2019**, *1347*, 012063. [CrossRef]
104. Cao, F.; Li, Z.; Zhang, N.; Ding, H.; Fuxiao, Y.; Liang, Z. Superplasticity, flow and fracture mechanism in an Al-12.7Si-0.7Mg alloy. *Mater. Sci. Eng. A* **2013**, *571*, 167–183. [CrossRef]
105. Gouthama; Padmanabhan, K.A. Transmission electron microscopy evidence for cavity nucleation during superplastic flow. *Scr. Mater.* **2003**, *49*, 761–766. [CrossRef]
106. Valiev, R.Z.; Langdon, T.G. Principles of equal-channel angular pressing as a processing tool for grain refinement. *Progr. Mater. Sci.* **2006**, *51*, 881–981. [CrossRef]
107. Chuvil'deev, V.N.; Kopylov, V.I.; Nokhrin, A.V.; Makarov, I.M.; Lopatin, Y.G. Dispersion limit upon equal-channel angular pressing. Temperature effect. *Dokl. Phys.* **2004**, *49*, 296–302. [CrossRef]
108. Perevezentsev, V.N.; Rybin, V.V.; Chuvil'deev, V.N. The theory of structural superplasticity: I. The physical nature of the superplasticity phenomenon. *Acta Metall. Mater.* **1992**, *40*, 887–894. [CrossRef]
109. Perevezentsev, V.N.; Rybin, V.V.; Chuvil'deev, V.N. The theory of structural superplasticity: III. *Boundary migration and grain growth, Acta Metall. Mater.* **1992**, *40*, 907–914. [CrossRef]
110. Chuvil'deev, V.N.; Nokhrin, A.V.; Pirozhnikova, O.E.; Gryaznov, M.Y.; Lopatin, Y.G.; Myshlyaev, M.M.; Kopylov, V.I. Changes in diffusion properties of nonequilibrium grain boundaries upon recrystallization and superplastic deformation of submicrocrystalline metals and alloys. *Phys. Solid State* **2017**, *59*, 1584–1593. [CrossRef]

111. Chuvil'deev, V.N.; Shavleva, A.V.; Nokhrin, A.V.; Pirozhnikova, O.E.; Gryaznov, M.Y.; Lopatin, Y.G.; Sysoev, A.N.; Melekhin, N.V.; Sakharov, N.V.; Kopylov, V.I.; et al. Influence of the grain size and structural state of grain boundaries on the parameter of low-temperature and high-rate superplasticity of nanocrystalline and microcrystalline alloys. *Phys. Solid State* **2010**, *52*, 1098–1106. [CrossRef]
112. Chuvil'deev, V.N.; Pirozhnikova, O.E.; Nokhrin, A.V.; Myshlyaev, M.M. Strain hardening under structural superplasticiy condition. *Phys. Solid State* **2007**, *49*, 684–690. [CrossRef]
113. Avtokratova, E.; Sitdikov, O.; Markushev, M.; Mulyukov, R. Extraordinary high-strain rate superplasticity of severely deformed Al-Mg-Sc-Zr alloy. *Mater. Sci. Eng. A* **2012**, *538*, 386–390. [CrossRef]
114. Komura, S.; Berbon, P.B.; Furukawa, M.; Horita, Z.; Nemoto, M.; Langdon, T.G. High strain rate superplasticity in an Al-Mg alloy containing scandium. *Scr. Mater.* **1998**, *38*, 1851–1856. [CrossRef]
115. Yuzbekova, D.; Mogucheva, A.; Kaibyshev, R. Superplasticity of ultrafine-grained Al-Mg-Sc-Zr alloy. *Mater. Sci. Eng. A* **2016**, *675*, 228–242. [CrossRef]
116. Lee, S.; Utsunomiya, A.; Akamatsu, H. Influence of scandium and zirconium on grain stability and superplastic ductilities in ultrafine-grained Al-Mg alloys. *Acta Mater.* **2002**, *50*, 553–564. [CrossRef]
117. Komura, S.; Horita, Z.; Furukawa, M.; Nemoto, M.; Langdon, T.G. Influence of scandium on superplastic ductilities in an Al-Mg-Sc alloy. *J. Mater. Res.* **2000**, *15*, 2571–2576. [CrossRef]
118. Perevezentsev, V.N.; Chuvil'deev, V.N.; Kopylov, V.I.; Sysoev, A.N.; Langdon, T.G. High-strain-rate superplasticity of Al-Mg-Sc-Zr alloys. *Russ. Metall.* **2004**, *1*, 28–35.
119. Likhachev, V.A.; Sen'kov, O.N. Effect of grain growth on superplasticity of alloys. *Strength Mater.* **1987**, *19*, 470–478. [CrossRef]
120. Perevezentsev, V.N.; Pirozhnikova, O.E.; Chuvil'deev, V.N. Grain growth during superplastic deformation of microduplex alloys. *Phys. Met. Metall.* **1991**, *71*, 29–36. (In Russian)
121. Chuvil'deev, V.N.; Nokhrin, A.V.; Makarov, I.M.; Lopatin, Y.G.; Sakharov, N.V.; Melekhin, N.V.; Piskunov, A.V.; Smirnova, E.S.; Kopylov, V.I. Solid solution decomposition mechanisms in cast and microcrystalline Al-Sc alloys: I. Experimental studies. *Russ. Metall.* **2012**, *5*, 415–427. [CrossRef]
122. Ocenasek, V.; Slamova, M. Resistance of recrystallization due to Sc and Zr addition to Al-Mg alloys. *Mater. Charact.* **2001**, *47*, 157–162. [CrossRef]
123. Jones, M.J.; Humphreys, F.J. Interaction of recrystallization and precipitation: The effect of Al_3Sc on the recrystallization behaviour of deformed aluminum. *Acta Mater.* **2003**, *51*, 2149–2159. [CrossRef]
124. Chuvil'deev, V.N.; Shadrina, Y.S.; Nokhrin, A.V.; Kopylov, V.I.; Bobrov, A.A.; Gryaznov, M.Y.; Shotin, S.V.; Tabachkova, N.Y.; Chegurov, M.K.; Melekhin, N.V. An investigation of thermal stability of structure and mechanical properties of Al-0.5Mg-Sc ultrafine-grained aluminum alloys. *J. Alloys Compd.* **2020**, *831*, 154805. [CrossRef]
125. Melton, K.N. The structure and properties of a cold-rolled and annealed Al-0.8 wt.%Zr alloy. *J. Mater. Sci.* **1975**, *10*, 1651–1654. [CrossRef]
126. Park, W.-W. Alloy design and characterization of rapidly solidified Al-Zr(-V) base alloys. *Mater. Des.* **1996**, *17*, 85–88. [CrossRef]
127. Røyset, J.; Ryum, N. Kinetics and mechanisms of precipitation in an Al-0.2 wt.% Sc alloy. *Mater. Sci. Eng. A* **2005**, *396*, 409–422. [CrossRef]
128. Hein, K.; Buhrig (Eds.) *Kristallisation aus Schmelzen*; Vew Deutscher Verlag Für Grundstoffindustrie: E. Leipzig, Germany, 1983; 356p. (In Germany)
129. Martin, J.W. *Micromechanisms in Particle-Hardened Alloys*; Cambridge University Press: Cambridge, UK, 1980; 167p.
130. Dorin, T.; Babaniars, S.; Jiang, L.; Cassel, A.; Eggeman, A.; Robson, J. Precipitation sequence in Al-Sc-Zr alloys revisited. *Materialia* **2022**, *26*, 101608. [CrossRef]
131. Tolley, A.; Radmilovic, V.; Dahmen, U. Segregation in Al_3(Sc,Zr) precipitates in Al-Sc-Zr alloys. *Scr. Mater.* **2005**, *52*, 621–625. [CrossRef]
132. Forbord, B.; Lefebvre, W.; Danoix, F.; Hallem, H.; Marthinsen, K. Three dimensional atom probe investigation on the formation of Al_3(Sc,Zr)-dispersoids in aluminium alloys. *Scr. Mater.* **2004**, *51*, 333–337. [CrossRef]
133. Fujikawa, S.I. Impurity diffusion of scandium in aluminum. *Defect Diffus. Forum* **1997**, *143–147*, 115–120. [CrossRef]
134. Kerkove, M.A.; Wood, T.D.; Sanders, P.G.; Kampe, S.L.; Swenson, D. The Diffusion coefficient of scandium in dilute aluminum-scandium alloys. *Metall. Mater. Trans. A* **2014**, *45*, 3800–3805. [CrossRef]
135. Peng, Y. Coarsening of Al_3Sc precipitates in Al-Mg-Sc alloys. *J. Alloys Compd.* **2019**, *781*, 209–215. [CrossRef]
136. Marwuis, E.A.; Seidman, D.N. Nanoscale structural evolution of Al_3Sc precipitates in Al(Sc) alloys. *Acta Mater.* **2011**, *49*, 1909–1919. [CrossRef]

Disclaimer/Publisher's Note: The statements, opinions and data contained in all publications are solely those of the individual author(s) and contributor(s) and not of MDPI and/or the editor(s). MDPI and/or the editor(s) disclaim responsibility for any injury to people or property resulting from any ideas, methods, instructions or products referred to in the content.